SCIENCE CHINA
Life Sciences

• RESEARCH PAPER •

Deficiency of betaine-homocysteine methyltransferase activates glucose-6-phosphate dehydrogenase (G6PD) by decreasing arginine methylation of G6PD in hepatocellular carcinogenesis

Jie Gao[1,2†], Xiao-Yi Shi[1,2†], Yao-Hui Sun[1,2†], Xu-Dong Liu[1,2], Feng Zhang[1,2], Cheng-Cheng Shi[2,3], Xiao Yu[1,2], Zhi-Ping Yan[1,2], Long Liu[1,2], Shi-Zhe Yu[4], Jia-Cheng Zhang[1,2], Xiao-Dan Zhang[1,2], Shui-Jun Zhang[1,2*] & Wen-Zhi Guo[1,2*]

[1]*Department of Hepatobiliary and Pancreatic Surgery, The First Affiliated Hospital of Zhengzhou University; Henan Diagnosis & Treatment League for Hepatopathy, The First Affiliated Hospital of Zhengzhou University; Henan Innovative Research Group for Hepatobiliary & Pancreatic Surgery and Digestive Organ Transplantation; Henan Organ Transplantation Quality Control Centre; Zhengzhou, Henan Province, 450052, China;*
[2]*Henan Engineering Technology Research Center for Organ Transplantation, Zhengzhou, Henan Province, 450052, China;*
[3]*Department of Pharmacy, The First Affiliated Hospital of Zhengzhou University, Zhengzhou, Henan Province, 450052, China;*
[4]*Department of General Surgery, Huashan Hospital, Fudan University; Cancer Metastasis Institute, Fudan University, Shanghai, 200040, China*

2023-09-08；2023-10-11

Betaine-homocysteine methyltransferase (BHMT) regulates protein methylation and is correlated with tumorigenesis; however, the effects and regulation of BHMT in hepatocarcinogenesis remain largely unexplored. Here, we determined the clinical significance of BHMT in the occurrence and progression of hepatocellular carcinoma (HCC) using tissue samples from 198 patients. BHMT was to be frequently found (86.6%) expressed at relatively low levels in HCC tissues and was positively correlated with the overall survival of patients with HCC. Bhmt overexpression effectively suppressed several malignant phenotypes in hepatoma cells *in vitro* and *in vivo*, whereas complete knockout of Bhmt ($Bhmt^{-/-}$) produced the opposite effect. We combined proteomics, metabolomics, and molecular biological strategies and detected that $Bhmt^{-/-}$ promoted hepatocarcinogenesis and tumor progression by enhancing the activity of glucose-6-phosphate dehydrogenase (G6PD) and PPP metabolism in DEN-induced HCC mouse and subcutaneous tumor-bearing models. In contrast, restoration of *Bhmt* with an AAV8-*Bhmt* injection or pharmacological inhibition of G6PD attenuated hepatocarcinogenesis. Additionally, coimmunoprecipitation identified monomethylated modifications of the G6PD, and BHMT regulated the methylation of G6PD. Protein sequence analysis, generation and application of specific antibodies, and site-directed mutagenesis indicated G6PD methylation at the arginine residue 246. Furthermore, we established bidirectionally regulated BHMT cellular models combined with methylation-deficient G6PD mutants to demonstrate that BHMT potentiated arginine methylation of G6PD, thereby inhibiting G6PD activity, which in turn suppressed hepatocarcinogenesis. Taken together, this study reveals a new methylation-regulatory mechanism in hepatocarcinogenesis owing to BHMT deficiency, suggesting a potential therapeutic strategy for HCC treatment.

HCC, BHMT, arginine methylation, G6PD, PPP metabolism

†Contributed equally to this work
*Corresponding author (email: ccguowz@zzu.edu.cn; zhangshuijun@zzu.edu.cn)

Introduction

Unrestrained proliferation of malignant cells is an important pathological basis for the occurrence and development of hepatocellular carcinoma (HCC) (Berardi et al., 2022; Li et al., 2021; Xu et al., 2020). However, the in-depth mechanisms of malignant proliferation remain unclear, leading to a lack of effective treatment measures to block hepatocarcinogenesis (Li et al., 2023b; Qi et al., 2021; Saw et al., 2021; Ti et al., 2021). Hyperactive glucose-6-phosphate dehydrogenase (G6PD) promotes oncogenesis and adaptive cross-drug tolerance by providing biosynthetic building materials and bolstering antioxidative defense (e.g., ribose-5-phosphate, NADPH, and glutathione) (Whitburn et al., 2022; Yamawaki et al., 2021; Zhang et al., 2021), emphasizing that the inhibition of abnormally activated G6PD may serve as a therapeutic strategy for tumors (Li et al., 2020; Min et al., 2022). Considering that post-translational modification (PTM) contributes to various biological functions, including regulation of Slug stabilization and G6PD overactivation (Dai et al., 2021; Ni et al., 2021; Teesalu et al., 2017; Zhu et al., 2021), we hypothesized if other PTMs, such as methylation of arginine residues, regulate G6PD activity and the pentose phosphate pathway (PPP).

Notably, as a very important and ubiquitous PTM of proteins, arginine methylation can regulate subcellular localization of proteins, affect their interactions, and control the activity of proteins, which plays a critical role in signal transduction and gene transcription—the processes that determine tumorigenesis and malignant proliferation of cells (Che et al., 2021; Liu et al., 2021; Tang et al., 2022; Yin et al., 2023). Arginine methylation has been implicated in oncogenesis. Defective methylation at arginine 159 weakens the phosphatase activity of phosphatase and tensin homolog deleted on chromosome 10 (PTEN) impair PTEN-mediated suppression of tumorigenesis (Feng et al., 2019). Deficiency in methylation of AKT1 at arginine 391 significantly suppresses its kinase activity to restrain tumorigenesis (Yin et al., 2021). Arginine methylation of BAG5 enhances its functional activity to repress tumorigenicity and cell survival of HCC (Che et al., 2021). However, the relationship between arginine methylation and G6PD function remains uncertain.

Betaine-homocysteine methyltransferase (BHMT), an important enzyme in the methionine cycle, is specifically overexpressed in hepatocytes and is implicated in the metabolism of S-adenosylmethionine—the key methyl donor required for protein and DNA methylation (Lee et al., 2023; Roy et al., 2020; Sternbach et al., 2021). BHMT regulates protein methylation and affects the function of modified proteins (Roy et al., 2020; Singh et al., 2021; Singhal et al., 2020), suggesting that it may be involved in regulating arginine methylation in G6PD. However, limited evidence has implicated BHMT in hepatocarcinogenesis. In patients of HCC with macrovascular invasion, proteomic signature has revealed that BHMT is remarkably downregulated in HCC (Cao et al., 2019); however, whether the relatively low expression of BHMT is a cause or consequence of hepatocarcinogenesis remains unknown. Seventy-eight-week-old *Bhmt*$^{-/-}$ mice are highly likely to develop neoplastic changes in the liver (Lupu et al., 2017). However, the role of endogenous BHMT in carcinogen-induced primary hepatocarcinogenesis has not been studied, and the underlying mechanisms of BHMT in hepatocarcinogenesis are largely unknown.

In this study, we aimed to uncover the role of BHMT in HCC. Moreover, we aimed to decipher the role of BHMT in G6PD methylation and its subsequent effect on PPP metabolism in hepatocarcinogenesis, to assess whether the BHMT/G6PD axis may serve as a potential therapeutic target for suppressing hepatocarcinogenesis.

Results

Frequently low BHMT expression correlated with poor prognosis in patients with HCC

To systematically test the profile of protein alterations in HCC, we first performed a comprehensive label-free proteomic study (Figure 1A–C) using liquid chromatography-mass spectrometry on tumor tis-

sues and corresponding paracancerous tissues from 40 patients with HCC. Hierarchical clustering revealed a dissimilar pattern of protein expression in non-cancerous liver tissues adjacent to the tumors (Figure 1A). Regarding important proteins that play an inhibitory role in liver cancer, we identified 56 proteins that were differentially expressed (> 2-fold difference, $P<0.05$) between tumor and paired non-tumor tissues (Figure 1B). Among the 10 top downregulated proteins (Figure S1A), BHMT attracted our attention because it impeded the development of liver cancer by regulating methylation of specific DNA loci. However, its protein methylation-related function in tumorigenesis remains unknown. BHMT level in HCC tissues was only 47.9% of that in paracancerous tissues (Figure 1C).

To further identify the correlation between BHMT and HCC tumorigenesis, other independent cohorts (Figure 1D–G) were analyzed. BHMT level in the cohort of paired HCCs (n=18) was 42.9% of that in paired adjacent non-cancerous tissues, as analyzed by western blotting (Figure 1D). Immunohistochemical (IHC) staining results (n=6) also showed low BHMT expression in tumor tissues (Figures 1E and S1B). Furthermore, tissue microarray immunohistochemistry of BHMT (n=134) revealed that up to 86.6% patients with HCC had decreased BHMT expression in tumor tissues compared with that in paired non-tumor tissues (Figure 1F, G). These results indicate that BHMT expression is frequently decreased in HCC and suggest a central role for BHMT in HCC tumorigenesis (Figure 1B–G). Remarkably, a low level of BHMT was significantly correlated with poor prognosis, as revealed by low overall survival (P=0.033) (Figure 1H). Additionally, 134 patients were divided into low-expression (n=67) and high-expression (n=67) groups based on BHMT expression. This revealed that alpha-fetal protein level (P=0.002) and microvascular invasion (P=0.045) were negatively related with BHMT expression (Table 1). Taken together, these findings indicate that BHMT deficiency accelerates hepatocarcinogenesis.

BHMT deficiency enhanced tumorigenicity of human hepatoma cells

We used *in vitro* and *in vivo* models to test whether the regulating of BHMT expression by genetic editing has therapeutic benefits or malignant effects on the tumorigenicity of human hepatoma cells. Consistent with the results of human clinical studies, *in vitro* experiments, such as cell viability and colony formation assays, showed that stable knockout of Bhmt (Bhmt$^{-/-}$) promoted proliferation of HuH7 and HepG2 cells (Figure 2A), which was reversed by stable overexpression of Bhmt (Figure 2B). In *in vivo* studies, HuH7 or HepG2 cells with manipulated BHMT were subcutaneously injected or orthotopically transplanted into nude mice to determine the role of BHMT in HCC development (Figure 2C–G). Overexpression of Bhmt resulted in a marked decrease in the ability of HuH7 and HepG2 cells to initiate tumor growth (Figure 2D–G). Conversely, knockout of Bhmt resulted in opposite effects in subcutaneous tumor-bearing and *in situ* tumor implantation models (Figure 2C, E–G). These results suggest that BHMT inhibits tumorigenicity of human HCC cells *in vitro* and *in vivo*.

***Bhmt* therapy alleviates tumorigenesis in diethylnitrosamine (DEN)-induced HCC model of mice**

BHMT is negatively associated with the tumorigenicity of human hepatoma cells. Therefore, verifying the role of BHMT in primary hepatocarcinogenesis and the actual therapeutic effect of *Bhmt* on primary liver cancer are important. We first explored whether the ablation of *Bhmt* (*Bhmt*$^{-/-}$) in mice using CRISPR/Cas9 might contribute to HCC tumorigenesis in a primary HCC model induced by intraperitoneal injection of DEN (Figure 3A, B). As excepted, NaCl-treated wild-type (WT) mice exhibited no spontaneous liver injury or malignancies at the age of 36 weeks, whereas NaCl-treated *Bhmt*$^{-/-}$ mice exhibited spontaneous liver injury; DEN-treated WT and *Bhmt*$^{-/-}$ mice developed typical HCC, as evident from gross anatomy of the liver and hematoxylin and eosin (H&E) staining (Figure 3C, D). Consistent with the results of previous clinical samples from patients with HCC, BHMT level was visibly reduced in DEN-induced HCC model, compared with that of NaCl-treated mice (Figures 3E and S1C), suggesting that overexpression of *Bhmt* might hamper HCC tumorigenesis. The liver/body weight ratio, tumor number, and maximum tumor volume were significantly higher in *Bhmt*$^{-/-}$ mice than in WT mice (Figure 3F). Together, these data imply that *Bhmt* therapy may have a promising effect on primary liver cancer.

To further elucidate the curative effect of *Bhmt* therapy in HCC development, Adeno-associated virus serotype 8 (AAV8)-Ctrl and AAV8-*Bhmt* were generated and respectively injected into DEN-treated *Bhmt*$^{-/-}$ mice (Figure 3G). DEN-induced primary HCC model was incorporated into *Bhmt*$^{-/-}$ mice, and all mice developed typical HCC. AAV8-*Bhmt* treatment substantially alleviated HCC tumorigenesis, which was accompanied by significantly increased BHMT levels in genetically altered mice (Figure 3H–J). Notably, some parameters, such as the liver/body weight ratio, tumor number, and maximum tumor volume, were significantly reduced in AAV8-*Bhmt* treated-mice as compared with those of AAV8-Ctrl treated mice (Figure 3K). The major findings from Figures 1 and 2 suggest that BHMT plays a suppressive role in HCC tumorigenesis.

Activated PPP and negative correlation between BHMT and G6PD in human HCC

BHMT plays vital roles in regulating glycometabolism (Garrido et al., 2018; Teng et al., 2012). Therefore, untargeted metabolomics was performed using tumor and corresponding paracancer tissues from patients with HCC, and significant changes were observed in most metabolites of PPP and other metabolic pathways, compared with those in non-tumor tissues (Figure 4A and Table S1). In particular, glyceraldehyde 3-phosphate (G3P), reduced nicotinamide adenine dinucleotide (NADH), erythrose 4-phosphate (E4P), ribulose 5-phosphate (Ru5p), and nicotinamide adenine dinucleotide phosphate (NADP) levels significantly increased in tumor tissues, whereas 1-deoxy-D-xylulose 5-phosphate (DOXP) level significantly decreased, implying that PPP was activated in HCC tissues (Figure 4A). Next, we examined whether activated PPP was related to the changes in metabolic enzymes in the metabolic pathway of PPP. The levels of G6PD, 6-phosphogluconolactose (PGLS), 6-phosphoglucote dehydrogese (PGD), ribose-5-phosphate isomerase (RPIA), ribulose-phosphate 3-epimerase (RPE), transketolase (TKT), and transaldolase (TALDO1) measured by label-free protein quantification were compared between HCC and non-tumor tissues. The results showed that the levels of G6PD, TKT, and RPE, but not of other enzymes in PPP, were markedly different in tumor tissues (Figure 4B). These results indicate that changes in G6PD, TKT, and RPE levels are closely related to PPP activation in HCC.

To assess the potential regulatory relationships between BHMT and activated PPP, we analyzed the correlation between BHMT and metabolic enzymes with changes in the PPP, and found that only G6PD and BHMT were negatively correlated in both adjacent noncancerous liver and tumor tissues (Figure 4C). Western blot analysis showed that G6PD level significantly increased in the cohort of HCC tissues (n=18), which is exactly opposite to the trend in BHMT (Figure 4D, E). For further verification, G6PD activity was measured using clinical samples of another batch from patients with HCC, and the results showed that G6PD activity was significantly enhanced in tumor tissues (n=28); specifically, 89.3% of patients with HCC had enhanced G6PD enzyme activity (Figure 4F, G). Taken together, these results suggest that BHMT may suppress HCC growth by inhibiting G6PD activity and PPP metabolism.

BHMT inhibits PPP metabolism and G6PD activity

BHMT was negatively correlated with G6PD expression and activity (Figure 4C–G); therefore, we tested the hypothesis that decreased BHMT might activate PPP by promoting G6PD expression or activity in HCC using DEN-induced HCC mouse model. Consistent with clinical results, G6PD expression and activity were significantly high in DEN-treated WT mice (Figure 5A, B). Moreover, BHMT was negatively correlated with G6PD expression and activity. Notably, in the absence of BHMT, G6PD expression and activity were significantly elevated in DEN-induce HCC model incorporated in *Bhmt*$^{-/-}$ mice compared to that in NaCl-treated mice (Figure 5A, B). G6PD activity was significantly upregulated; however, its expression was not altered in *Bhmt*$^{-/}$ mice, compared with that in WT mice. Likewise, compared with those in DEN-treated WT mice, the changes in G6PD expression and activity in DEN-treated *Bhmt*$^{-/-}$ mice were similar to that in NaCl -treated *Bhmt*$^{-/-}$ mice (Figure 5A, B). In line with the major conclusions from Figures 3 and 4, these results indicate that upregulated G6PD activity, but not its expression, is negatively modulated by BHMT, thereby strongly promoting hepatocellular carcinogenesis

in DEN-induced mouse model.

Furthermore, overexpression or knockdown of Bhmt in both HuH7 and HepG2 cells did not alter G6PD expression (Figure 5C). Notably, increased level of BHMT resulted in relatively low G6PD activity compared to that in the WT. Consequently, PPP was significantly downregulated, as shown by the diminished 6PG content and ratio of NADPH to $NADP^+$, and levels of reactive oxygen species (ROS) significantly increased in cells overexpressing BHMT, compared with that in control cells (WT) (Figure 5D). In contrast, deletion of Bhmt in HuH7 and HepG2 cells upregulated G6PD activity, which might promote PPP metabolism and inhibit intracellular ROS generation (Figure 5D). The mouse xenograft tumor model showed that BHMT expression was negatively correlated with G6PD activity; however, it did not affect G6PD expression, consistent with the negative correlation between BHMT expression and PPP metabolism (Figure 5E, 5F).

In summary, these data reveal a regulatory mechanism that reduces BHMT levels and stimulates hepatocarcinogenesis by controlling G6PD activity and regulating PPP metabolism.

BHMT alleviates oncogenesis by inhibiting G6PD activity and PPP metabolism

BHMT expression was negatively associated with G6PD activity, but not G6PD expression (Figure 5), suggesting that the loss of BHMT promotes HCC by inducing G6PD activity. To this end, 6-aminonicotinamide (6AN), a pharmacological inhibitor of G6PD, and a genetic G6PD knockdown method were used to inhibit hyperactive G6PD activity owing to BHMT deficiency during tumor formation and proliferation.

6AN significantly inhibited G6PD activity in WT cells, compared with that in the solvent control (Sol.), accompanied by reduced levels of 6PG and NADPH/$NADP^+$ (Figure 6A). Consistently, pharmacological inhibition of G6PD ($Bhmt^{-/-}$ + inhibitor) also attenuated G6PD activity and the levels of 6PG and NADPH/$NADP^+$ and increased intracellular ROS levels, compared with those of the control ($Bhmt^{-/-}$ + Sol.) (Figure 6A). However, chemical inhibition of G6PD in HepG2 cells overexpressing Bhmt did not remarkably suppress G6PD activity, presumably owing to adequate BHMT expression to inhibit G6PD activity, which significantly moderated the inhibitory effects of 6AN (Figure 6A). To test the idea that G6PD activation by Bhmt deletion may upregulate PPP metabolism for HCC proliferation, we used 6AN, which substantially decreased the growth and clone formation of WT hepatoma cells (Figure 6B). Treatment of $Bhmt^{-/-}$ cells by 6AN reduced the rapid tumor growth caused by BHMT deficiency *in vitro*, which was characterized by diminished cell viability and clone formation, compared with those of the Sol. group (Figure 6B). Silencing of G6PD in $Bhmt^{-/-}$ cells ($Bhmt^{-/-}$ + shG6PD) attenuated G6PD activity and the levels of 6PG and NADPH/$NADP^+$ and increased intracellular ROS, compared with that of the control group ($Bhmt^{-/-}$ + shNC) (Figure S2A, B). Furthermore, rapid tumor proliferation *in vitro*, including cell viability and clone formation was significantly reduced (Figure S2C).

To test whether G6PD inhibition by 6AN-induced BHMT deficiency might be pharmaceutically beneficial for oncogenicity of human HCC cells *in vivo*, we applied 6AN in a nude mouse xenograft model. WT and $Bhmt^{-/-}$ hepatoma cells were inoculated into nude mice via subcutaneous injection, which were then intraperitoneally injected with 6AN or Sol. (Figure 6C). The results showed that the 6AN treatment rapidly decreased tumor oncogenicity, characterized by reduced tumor volume, compared with that of the Sol. group (Figure 6D). Furthermore, G6PD activity, 6PG level, and the ratio of NADPH to $NADP^+$ were significantly reduced by 6AN treatment (Figure 6E). Together, these data clearly demonstrate that BHMT deficiency promotes liver oncogenesis by enhancing G6PD activity and PPP metabolism; however, pharmacological targeting-induced G6PD activity and activated PPP metabolism owing to BHMT deficiency attenuate liver tumorigenesis.

BHMT represses G6PD activity by enhancing arginine methylation in G6PD

Arginine methylation plays a vital role in regulating protein activity, and G6PD activity is influenced by PTM; however, arginine methylation of G6PD has not been examined. To test the hypothesis that

BHMT, an enzyme regulating protein methylation, inactivates G6PD, we analyzed arginine methylation of G6PD in hepatoma carcinoma cells by immunoprecipitation of endogenous G6PD, followed by immunoblotting using an anti-monomethyl arginine (R*GG) antibody. The results showed that G6PD was readily methylated in HuH7 and HepG2 cells (Figure 7A). Bhmt overexpression significantly enhanced arginine methylation of G6PD; which was remarkably suppressed owing to Bhmt deficiency in both HuH7 and HepG2 cells (Figure 7A), suggesting that arginine methylation of G6PD can be regulated by BHMT. Moreover, to identify the arginine methylation sites, G6PD sequences from multiple species were aligned, which showed that arginine at position 246 (R246) was well conserved across species (Figure 7B). Accordingly, we generated and unmodified peptide fragment (amino acid 240-252) and peptide fragment monomethylated at R246 to generated a site-specific antibody against methylated R246. The site-specific antibody showed higher specificity in the dot blot assay than did the site-nonspecific antibody (Figure 7B). Notably, R246 is the only putatively available residue for mono-methylation in human G6PD. Accordingly, R246 was mutated to lysine (R246K) in G6PD, which was used as mimetic that cannot be methylated (Figure 7C); notably, R246K mutation abolished arginine methylation in HuH7 and HepG2 cells, compared with that in WT hepatoma cells (Figure 7D). In addition, we determined the extent of arginine methylation in hepatoma cells transfected with vector (Vec), WT, or R246K plasmids, and found that R246K mutation eliminated G6PD methylation (Figure 7E). Furthermore, mass spectrometry identified a methylated arginine residue (R2246) in G6PD (Figure 7F and Table S2), demonstrating that R246 is a specific site of methylation in G6PD.

To elucidate whether R246 methylation of G6PD was related with BHMT expression, G6PD-Vec, G6PD-WT, and G6PD-R246K were expressed in control (WT), deficient ($Bhmt^{-/-}$), and overexpressed (Bhmt) hepatoma cells, respectively, and the results showed that Bhmt knockout virtually abolished R246 methylation of G6PD in HuH7 and HepG2 cells (Figure 8A). Conversely, ectopic expression of BHMT augmented endogenous R246 methylation of G6PD (Figure 8A). Next, we examined whether R246 methylation was relevant to G6PD activity and PPP metabolism. G6PD-R246K exhibited significantly higher G6PD activity and PPP metabolism than did G6PD-Vec and G6PD-WT (Figure 8B, C), which was also supported by the finding that G6PD activity, 6PG content, and $NADPH/NADP^+$ were enhanced upon Bhmt knockout and inhibited once Bhmt was overexpressed, whereas intracellular ROS levels showed opposite trends (Figure 8B, C). These data demonstrate that BHMT represses G6PD activity by enhancing R246 methylation of G6PD in HCC.

R246K mutation improved the proliferation and cloning of HuH7 and HepG2 cells (Figure 8D) and reversed the proliferation of tumor cells caused by overexpressed BHMT (Figure S2D). Furthermore, R246 methylation of G6PD was drastically decreased in tumors (Figure 8E), and a positive correlation between BHMT and methylation levels (Figure 8F) and a negative association between R246 methylation and tumor node metastasis (TNM) staging (Figure 8G) were noticed. Furthermore, R246 methylation of G6PD was positively associated with the overall survival of patients with HCC (Figure 8H), and patients with HCC and low levels of R246 methylation and BHMT had the shortest overall survival (Figure 8I). Taken together, BHMT exhibits a novel tumor-suppressive role by enhancing R246 methylation of G6PD, thereby inhibiting G6PD activity and PPP metabolism.

Discussion

Arginine methylation regulated by protein arginine methyltransferases has been explored in detail (Koh et al., 2015; Li et al., 2023a; Zhou et al., 2023); however, the link between arginine methylation and metabolic enzymes regulating the synthesis of methyl donors is relatively weak compared with those for other protein arginine methyltransferases (Kim et al., 2023; Shi et al., 2023; Zhang et al., 2023). This study shows that G6PD, a key driver of HCC, was methylated at R246, which negatively regulated PPP metabolism by reducing G6PD activity. Notably, arginine methylation was manipulated by BHMT expression. Moreover, BHMT level was significantly low in human HCC tissues and was positively asso-

ciated with overall survival. Accordingly, restoration of *Bhmt* expression led to a reduced hepatocarcinogenesis phenotype, and intervention treatment with 6AN, an inhibitor of G6PD, counteracted enhanced tumorigenesis owing to BHMT deficiency. Overall, BHMT suppressed HCC by acting regulating R246 methylating of G6PD.

BHMT, an enzyme predominantly distributed in the liver, plays essential roles in regulating one-carbon metabolism and influencing hepatic lipid accumulation, which has various functions in folate cycle (Grzelj et al., 2021), oscillatory homocysteine homeostasis (Tsuchiya et al., 2015), lipid synthesis (Li et al., 2022b), gluconeogenesis (Shen et al., 2019), and choline metabolism (Teng et al., 2011). Interestingly, an isobaric tag for relative and absolute quantitation (iTRAQ)-based proteomic study has found decreased BHMT level in patients with HCC having macrovascular Invasion (Cao et al., 2019). Our study found that BHMT level was lower in HCC tissues than in paired nontumor tissues. In addition, patients with HCC having low BHMT expression had poor overall survival. Therefore, BHMT plays an important role in hepatocarcinogenesis.

DEN-induced HCC is similar to HCC in humans (Haberl et al., 2021). In addition, DNE is widely found in products, such as processed meats (Qiu et al., 2017), food color additives (Zeng et al., 2022), tobacco smoke (Gupta et al., 2010), and whiskey (Owumi et al., 2021). To the best of our knowledge, this is the first study to demonstrate the protective effect of BHMT on DEN-induced primary hepatocarcinogenesis and highlight the therapeutic potential for hepatocarcinogenesis by targeting BHMT or Bhmt through gene editing for treating solid tumors (Li et al., 2022a; Yin et al., 2022). To facilitate tumor oncogenicity, deficient BHMT has been shown to alter the methylation of specific DNA loci to repress the expression of Iqgap2 and F2rl2, resulting in development of preneoplastic foci in the liver. Whether BHMT is involved in regulating arginine methylation of proteins, which might be beneficial for hepatocarcinogenesis, warrants further investigation.

Overactivated G6PD is associated with hepatocarcinogenesis and malignant cell growth (Cao et al., 2021; Whitburn et al., 2022; Zhang et al., 2021). However, the inhibition of G6PD activity and PPP metabolism has not produced satisfactory clinical outcomes owing to an incomplete understanding of the mechanisms underlying the regulation of G6PD activity. We found that upregulated G6PD was negatively associated with low BHMT levels in human HCC and nontumor tissues, and that G6PD activity was significantly elevated in HCC tissues, implying an intimate relationship between BHMT and G6PD. The loss of BHMT resulted in enhanced G6PD activity, but not G6PD expression. This is consistent with previous observations that the regulation of G6PD expression and activity are two related but independent regulatory processes (Ni et al., 2021), extending the evidence that the elimination of BHMT exacerbates hepatocarcinogenesis by manipulating G6PD activity. In our study, pharmacological inhibition of G6PD activity and PPP metabolism inhibited the growth of human liver neoplasms owing to the loss of BHMT, implying a viable therapeutic opportunity for HCC by targeting G6PD activity and PPP metabolism.

G6PD activity is mainly regulated by PTM (Wang et al., 2019; Wang et al., 2014); specifically, phosphorylation, acetylation, glycosylation, and glutarylation alter the G6PD activity (Teesalu et al., 2017; Zhou et al., 2016), emphasizing that understanding PTM of G6PD, particularly the undefined modification types, might be valuable for targeting tumorigenesis owing to hyperactive G6PD. Arginine methylation as an epigenetic modulator plays an important role in protein function (Liu et al., 2022). For example, arginine methylation of Mxi1 confers radioresistance to non-small cell lung cancer cells by decreasing Mxi1 stability (Yang et al., 2022). BHMT plays an essential role in directly catalyzes the formation of methionine, the precursor of S-adenosylmethionine, and is involved in the regulating protein methylation (Lupu et al., 2017; Wojtala et al., 2021). Therefore, BHMT may inhibit G6PD activity by modulating G6PD methylation. Notably, we found that R246 of G6PD was methylated, and that the level of R246-methylated G6PD was regulated by expression status of BHMT. Moreover, G6PD activity was mediated by its methylation, and BHMT was involved in the regulatory process. Therefore, the

BHMT–G6PD axis plays a vital role in regulating HCC tumorigenicity, although we cannot rule out other possibilities.

BHMT is frequently underexpressed in HCC; therefore, its restoration is an effective strategy for targeting hepatocarcinogenesis. Our data suggest that *Bhmt* therapy alleviates HCC tumorigenesis. Another outstanding feature of BHMT is that it is a regulator of arginine methylation of G6PD, and its absence results in reduced G6PD activity, highlighting that G6PD inhibition owing to the absence of BHMT may be a favorable therapeutic strategy for HCC, as was indicated by our findings. This study highlights the importance of BHMT expression and arginine methylation of G6PD in HCC and clearly indicates that targeting BHMT-mediated PTM of proteins might be a promising therapeutic strategy for treating HCC.

Materials and methods

Human HCC samples

This study was conducted in accordance with the Declaration of Helsinki and was approved by the Clinical Research Ethics Committee of First Affiliated Hospital of Zhengzhou University. Written informed consent was obtained from all patients with HCC included in the study, according to the policies of the ethics committee. The study was conducted in 198 patients with HCC, including 58 pairs of fresh tissue and 140 pairs of paraffin-embedded samples. All specimens were pathologically confirmed at the same hospital.

Antibodies, reagents and plasmids

Antibody against BHMT (NBP2-75418), G6PD (ab993, ab91034), Flag (bsm-33346M), β-Actin (20536-1-AP, 66009-1-Ig), and R*GG were purchased from Novus Biologicals, Abcam, Bioss antibodies, Proteintech Group, Inc., and Cell Signaling Technology, respectively. Site-specific antibodies against monomethylated R246 (G6PD-R246 me1) and unmethylated R246 (G6PD-R246) were generated by absin Bioscience Inc.. Goat anti-mouse IgG H&L (HRP) (ab6789) and goat anti-rabbit IgG H&L (HRP) (ab6721) antibodies were purchased from Abcam. Diethylnitrosamine (DEN, No258) and polybrene (H9268) were purchased from Sigma-Aldrich, and 6-aminonicotinamide (6AN, S9783) was purchased from Selleck (Shanghai, China). Puromycin (A1113803) was purchased from Gibco (Grand Island, NY). Lipofectamine™ 3000 transfection reagent (L3000015) was purchased from Thermo Fisher Scientific. The expression plasmids pLenti-CMV-GFP-Puro (CD513B-1), psPAX2, and pMD2.G were purchased from the Public Protein/Plasmid Library (PPL, Nanjing, China). Bhmt cDNA was synthesized by Sangon Biotech Co., Ltd and cloned into the pLenti-CMV-GFP-Puro Vec. WT G6PD (G6PD-WT) and mutant G6PD (G6PD-R246K), generated using phanta Max-Super-Fidlity DNA polymerase (Vazyme), were subcloned into pcDNA3.1-CMV-MCS-3flag-EF1-ZsGreen-T2A-Puro. ShG6PD#1 (GCCTTCCATCAGTCGGATA), shG6PD#2 (GTCGTCCTCTATGTGGAGAAT), shG6PD#3 (CAACAGATACAAGAACGTGAA) and shNC (GTTCTCCGAACGTGTCACGTT) were synthesized by Public Protein/Plasmid Library and cloned into pPLK-GFP-Puro Vec. To generate Bhmt knockout HuH7 and HepG2 cells, small guide RNA (sgRNA) sequences (sgRNA-1, GATCCTAGAACGTTTAAATGCTGG; sgRNA-2, GAAGAGGGGCTACGTAAAGGCAGG, and sgRNA-3, GTCTATTGTAAGTTCTCATAAAGG) for CRISPR/Cas9 were designed by CRISPR design website (http://crispr.mit.edu/) (Huang et al., 2019). The sgRNA-1 and sgRNA-2 target exon 2, and sgRNA-3 targets intron 2 of Bhmt. The complementary oligonucleotides for sgRNAs were annealed and cloned into pX459 CRISPR/Cas9-Puro Vec (Addgene).

Cell culture and transfection

HEK293T, HuH7, and HepG2 cell lines were obtained from the American Type Culture Collection and cultured in Dulbecco's Modified Eagle Medium supplemented with 10% fetal bovine serum (Gibco).

The cell culture medium contained 100 μg/ml streptomycin and 100 units/ml penicillin. Cells were incubated under 5% CO_2 at 37 °C. Lipofectamine 3000 was used for transfection according to the manufacturer's instruction. HEK293T cells were co-transfected with lentiviral packaging plasmids (psPAX2 and pMD2.G) and the indicated plasmids for 48 h. Supernatant of HEK 293T cells were collected and used to infect HuH7 and HepG2 cells with polybrene (10 μg/ml). Infected HuH7 and HepG2 cells were treated with puromycin (2 μg/ml) to obtain acquire stable cell lines.

Establishment of knockout cell lines using CRISPR/Cas9

HEK293T cells were co-transfected with BHMT/sgRNA-1, BHMT/sgRNA-2, and BHMT/sgRNA-3，as previously described (Zhou et al., 2022). Two days after transfection, single cells were sorted using flow cytometry and cultured for 7–10 days until colonies appeared. Single colonies were selected and screened by polymerase chain reaction (PCR) and agarose gel electrophoresis. PCR primers (TCTGGTTGTTTGTCTTATAGATAGCCATA and GGTTTCCATCAATTCTAGCTACCAC) were designed for Bhmt deletion. Sanger sequencing and western blot analysis were performed for further verification.

6AN incubation

HuH7 and HepG2 cells were cultured in a medium containing 25μM 6AN or Sol.. The medium was replaced every 48 h. For enzymatic activity assay of G6PD, and quantification of PPP metabolites, and cell proliferation assay, and clone formation assay, hepatoma cells were cultured with 6AN or Sol. for 4, 5, and 14 days, respectively.

In vitro cell proliferation assay

Hepatoma cells, including knockout cell lines and cells transfected with the designed plasmids, were seeded in sextuplicate at 2000 cells/well in a 96-well plate. After 24 h, cells were treated with vehicle alone or 25μM 6AN. Cell viability was measured using a Cell Counting Kit-8 (CCK-8, B34304; Bimake). For colony formation, hepatoma cells were seeded in triplicate at 3000 cells/well in a 6-well plate and grown for 14 days. Cells were fixed with 4% paraformaldehyde, stained with 0.1% crystal violet, and photographed using a ChemiDoc XRS (Bio-Rad).

Western blot analysis

Liver tissues or cells were lysed with RIPA lysis buffer (R0010; Solarbio Life Sciences) or Native lysis Buffer (R0030; Solarbio Life Sciences) containing protease inhibitors for protein extraction. The supernatant was collected and quantified using a bicinchoninic acid protein assay kit (23225; Thermo Fisher Scientific), and western blotting was performed to analyze protein expression. The indicated primary antibodies were used for immunoblotting, and proteins transferred to polyvinylidene fluoride membranes were detected using a chemiluminescent HRP substrate (Millipore) in an Amersham ImageQuant 800 (Amersham). Band intensity was quantified using Image J software (National Institute of Health, Bethesda, MD, USA).

Tissue microarray and immunohistochemistry

IHC staining for BHMT and R246 methylation of G6PD and image analysis were performed as previously described (Gao et al., 2020). HCC tissues were obtained immediately after hepatectomy, fixed in 10% formalin and embedded in paraffin. IHC staining was scored by calculating the histochemistry score (H-Score) by the following formula: Percentage of cells of weak intensity ×1 + percentage of cells of moderate intensity ×2 + percentage of cells of strong intensity ×3. Scanning and analysis of IHC slides and tissue microarray were performed using CaseViewer v.2.4 (3DHISTECH) and Quant Center v.2.1 (3DHISTECH) to quantify protein expression.

Proteomic analysis

According to previous study (Seyfried et al., 2008), for label-free quantitative mass spectrometry, proteins were extracted using SDT [4% (w/v) sodium dodecyl sulfate (SDS), 100 mM Tris/HCl (pH 7.6), and 0.1 M dithiothreitol (DTT)], and quantified using a bicinchoninic acid protein assay kit. Appropriate proteins were extracted from samples for trypsin hydrolysis using the filter-aided sample preparation (FASP) method. A C18 cartridge was used to desalinate peptides. After lyophilization, peptides were redissolved in 40 μL of 0.1% formic acid solution and quantified at 280nm. Each sample was separated into 15 fractions by reverse-phase high-performance liquid chromatography (RP-HPLC), and combined into 5 fractions using the orthogonal combination method. Liquid chromatography–tandem mass spectroscopy (LC-MS/MS) was performed using a Q Exactive mass spectrometer (QE-HF-X; Thermo Fisher Scientific) coupled with Nano-LC (Easy1200; Thermo Fisher Scientific). Peptides were loaded onto a reverse-phase trap column (Acclaim PepMap 100 C18 Nano Viper, 100 μm × 2 cm; Thermo Fisher Scientific) connected to a C18-reversed phase analytical column (EASY-Column, 10 cm length, 75 μm inner diameter, and 3μm resin; Thermo Fisher Scientific) in buffer A (0.1% formic acid) and separated with a linear gradient of buffer B (84% acetonitrile and 0.1% formic acid) at a flow rate of 300 nL/min controlled by IntelliFlow technology. The mass spectrometer was operated in the positive ion mode.
MS data were acquired using a data-dependent top10 method by dynamically choosing the most abundant precursor ions from the survey scan (300–1800 m/z) for HCD fragmentation. The automatic gain control target was set to $1e^6$, and the maximum injection time was set to 50 ms. The duration of dynamic exclusion was 60 s. Survey scans were acquired at a resolution of 70000 at m/z 200; the resolution for HCD spectra was set to 17500 at m/z 200; and the isolation width was 2 m/z. The normalized collision energy was 30 eV, and the underfill ratio, which specifies the minimum percentage of the target value likely to be reached at the maximum fill time, was defined as 0.1%. The instrument was run in the peptide recognition mode. The raw MS data for each sample were combined and searched using MaxQuant v.1.5.3.17 software for identification and quantitation.

Generation of *Bhmt*$^{-/-}$ mice and induction of HCC model and gene therapy

All animals received human care, and the study protocols were approved by the Animal Ethics Committee of our department. A *Bhmt*$^{-/-}$ C57BL/6 mouse model was generated by CRISPR/Cas9 mediated gene-specific knockout, as previously described (Chao et al., 2019; Huang et al., 2019), and mouse genotyping was performed by DNA sequencing and PCR. Four sgRNAs (TATAATTTCTTTAGCACCCTTGG, TCCCCTGAATTTACAGATGAGGG, AGCGTGTACCAACCTGCCTCAGG, and CACATCATCATAGTTTAGAATGG) and PCR detection primers (GGCTCTGGGTTTGCAACATTT and CAGGATCAATACCAGGGACGG) were designed for *Bhmt* deletion. To induce primary HCC, *Bhmt*$^{-/-}$ and *Bhmt* WT male mice were injected with a single dose of DEN (25 mg/kg) or normal saline (NaCl) on postnatal day 14. After mice were sacrificed at the age of 36 weeks, the liver, tumor tissues, and plasma were collected. To investigate the tumor-suppressive role of BHMT, *Bhmt*$^{-/-}$ mice with DEN-induced HCC were injected with AAV8-*Bhmt* or AAV8-Ctrl (Hanbio Biotechnology Co., Ltd., Shanghai, China) through the tail vein at weeks 16 and 26. Mice were sacrificed at the age of 36 weeks, and liver tissues and plasma were collected.

Xenografts tumor models

For the subcutaneous xenograft model, BALB/c nude mice (male, five-weeks-old) were randomly grouped (n=5 per group). A total of 5×10^6 hepatoma cells, including knockout cell lines and cells transfected with the designed plasmids, were subcutaneously injected into the right or left flank of mice, as shown in Figures 2 and 6. Mice were administered 6AN (3mg/kg) or solvent only by intraperitoneal injection every other day from day 6 of modeling (n=5 per group). Seven days after implantation, tumor volume was measured every two days and calculated by the formula, length × width × width/2. Four

weeks after subcutaneous injection, mice were euthanized, and tumor tissues were dissected.

For the orthotopic model, tumor blocks obtained from the subcutaneous xenograft model were cut into small pieces of approximately 1.0 mm^3 in phosphate-buffered saline. After anesthesia with sodium pentobarbital through intraperitoneal administration, nude mice were subjected to left upper abdominal transverse incision to expose the liver. Within 40 min of tumor isolation, two small tumor masses were implanted in the deep parenchyma of the right liver lobe using a thick needle. The incision was quickly sewn with a medical suture and a suture needle. Mice were sacrificed after 5 weeks.

Untargeted metabolomics

To extract metabolites from the liver (Jin et al., 2020), 1 mL of cold extraction solvent containing methanol/acetonitrile/H_2O (2:2:1, v/v/v) was added to 80 mg sample and adequately vortexed. The lysate was homogenized using an MP homogenizer (24×2, 6.0 M/S, 60 s, twice), sonicated at 4 °C (30 min/once, twice), and centrifuged at 14000 ×g for 20 min at 4 °C, and the supernatant was dried in a vacuum centrifuge at 4 °C. For LC-MS analysis, the samples were redissolved in 100 μL acetonitrile/water (1:1, v/v). LC-MS analysis was performed using a quadrupole time-of-flight mass spectrometer (Sciex TripleTOF 6600) coupled to hydrophilic interaction chromatography via electrospray ionization (ESI) in the positive and negative modes. The ESI source conditions were set as follows: ion source gas 1 (gas 1) as 60, ion source gas 2 (gas 2) as 60, curtain gas as 30, source temperature at 600 ℃, IonS
Floating ± 5500 V. For MS acquisition, the instrument was set for acquision over an m/z range of 60–1000 Da, and the accumulation time for TOF MS scan was set at 0.20 s/spectra. In auto-MS/MS acquisition, the instrument was set for acquisition over an m/z range 25–1000 Da, and the accumulation time for product ion scan was set at 0.05 s/spectra. The product ion scan was acquired using information-dependent acquisition with high-sensitivity mode. The parameters were set as follows: collision energy was fixed at 35 V with ± 15 eV; declustering potential, 60 V (+) and −60 V (−); exclusion of isotopes within 4 Da; and candidate ions to monitor per cycle, 10. Raw MS data (wiff.scan files) were converted into MzXML files using ProteoWizard MSConvert before being imported into the freely available XCMS software. The following parameters were used for peak selection: centWave m/z, 25 ppm; peak width, c (10, 60); and prefilter, c (10, 100). For peak grouping, the parameters were bw, 5; mzwid, 0.025; minfrac, 0.5. In the extracted ion features, variables with > 50% non-zero measurement values in at least one group were kept. Compound identification of metabolites by MS/MS was performed using an in-house database established by Shanghai Applied Protein Technology Co., Ltd. with available authentic standards.

Assay of G6PD activity and quantification of PPP metabolites

G6PD activity was assayed using a G6PD Kit, as previously reported (Ma et al., 2021). Briefly, proteins from liver or cell lysates were quantified using a bicinchoninic acid protein assay kit (23225, Thermo Fisher Scientific), according to the manufacturer's instructions. G6PD activity was determined based on the concentration of NADPH in the reaction system and calculated from the difference between NADPH concentrations at the beginning (0 min) and end (5 min) of the reaction. Based on the metabolomic and proteomic data, the contents of 6PG and NADPH/$NADP^+$ in cells or tumor tissues were measured as previously described, using colorimetric or fluorometric kits from Abcam (ab 211071) and Sigma-Aldrich (MAK312) (Liu et al., 2019).

ROS measurement

Changes in ROS levels were measured using a fluorescent probe dihydroethidium (UElandy) according to the manufacturer's instructions. Briefly, cells were seeded in 96-well plates at 70–80% confluence and incubated with the fluorescent probe. After 2 h, fluorescence was measured at 535 and 590 nm using a VARIOSKAN LUX Multi-Mode Microplate Reader (Thermo Fisher Science). ROS levels were normal-

ized with respect to that of the control group.

Co-immunoprecipitation (coIP)

For coIP of G6PD, cells were lysed using Native lysis Buffer containing protease inhibitors. Whole-cell lysates at equal concentrations and volumes were incubated with primary antibody or IgG, and G6PD was pulled down using protein A/G Sepharose beads (7Sea Pharmatech Co.,Ltd). The precipitated protein complexes were washed five times with Native lysis Buffer, separated using SDS-polyacrylamide gel electrophoresis, transferred onto membranes and immunoblotted using the indicated antibodies.

Generation of antibody against R246 me1 and dot blot assay

Amino acid sequences of peptides corresponding to the 240-252 region (PFGTEGRGGYFD) of G6PD, in which R246 was unmodified or monomethylated, were generated by Absin Bioscience Inc.. Anti-G6PD-R246 or anti-G6PD-R246 me1 antibodies were obtained by immunizing rabbits with synthetic unmodified or monomethylated peptides. Methylated and unmethylated peptides at different amounts were spotted onto nitrocellulose membranes and detected using control anti-G6PD-R246 or anti-G6PD-R246 me1 antibodies.

Detection of methylated proteins

To identify the methylated site in G6PD, lysate of HuH7 cells overexpressing Bhmt was immunoprecipitated using anti-G6PD antibody, and the samples were sent to Shanghai Bioprofile (Shanghai, China) for methylation mass spectrometry analysis. Briefly, the bound proteins were extracted from IP beads using SDT lysis buffer (pH 8.0). IP beads were boiled for 5 min and ultrasonicated. Undissolved beads were removed by centrifugation at 16000 ×g for 15 min, and the supernatant containing the proteins was collected. Proteins were digested using the FASP method (Wisniewski et al., 2009). Specifically, proteins were digested using 6 μg chymotrypsin in 40 μL NH_4HCO_3 buffer overnight at 25 °C. The peptides were collected by centrifugation at 12000 ×g for 10 min and then desalted using C18 StageTip for LC-MS analysis.

LC-MS/MS experiments were performed using a Q Exactive HF-X mass spectrometer coupled to an Easy nLC1200 (Thermo Fisher Scientific). The Peptides were first loaded onto a trap column (100 μm × 20 mm, 5 μm, C18; Dr. Maisch GmbH, Ammerbuch, Germany) in buffer A (0.1% formic acid in water) and buffer B (0.1% formic acid in 80% acetonitrile). RP-HPLC separation was performed using a self-packed column (75 μm × 150 mm, 3 μm ReproSil-Pur C18 beads, 120 Å; Dr. Maisch GmbH) at a flow rate of 300 nL/min. The gradient was set as follows: 2–5% buffer B between 0–2 min, 5–28% buffer B between 2–44 min, 28–40% buffer B between 44–51 min, 40–100% buffer B between 51–53 min, and 100% buffer B till 60 min. MS data were acquired using a data-dependent top20 method by dynamically choosing the most abundant precursor ions from the survey scan (350–1800 m/z) for HCD fragmentation. A lock mass of 445.120025 Da was used as the internal standard for mass calibration. Full MS scans were acquired at a resolution of 60000 at m/z 200, and 15000 at m/z 200 was used for MS/MS scan. The maximum injection times were set to 50 ms for MS and 25 ms for MS/MS. The normalized collision energy was 28, and the isolation window was set to 1.6 m/z. The scores and reliability of each site were obtained by analyzing the abundance of peptide segments and frequency of methylated sites., Peptides with at least seven amino acids were required for identification.

Statistical analysis

A hierarchical algorithm was used to cluster differentially expressed proteins in tumor and adjacent non-cancerous liver tissues, and the data were displayed by a heatmap. Differentially expressed proteins

screened by multiple change > 2 times (upregulated by > 2 times or downregulated by < 0.5) and *P*-value <0.05 (Student's *t*-test) effectively separated the two groups, and the quantitative results of proteins were displayed by volcano plots. The Kaplan–Meier analysis and log-rank test were used to compare overall and recurrence-free survival of different groups. Student's *t*-test (two-tailed) was used for statistical analysis between two groups; one-way analysis of variance (ANOVA) followed by two-tailed unpaired Student's *t*-test was used for multiple comparisons. A paired-sample *t*-test was performed to compare differences between paired samples. Significant correlations were determined using two-tailed Pearson correlation. A *P*-value < 0.05 was considered statistically significant. All graphs were generated using Photoshop CC v.2014 (Adobe, San Jose, CA, USA) and GraphPad Prism v.5.04 (GraphPad Software, La Jolla, CA, USA).

Compliance and ethics *The authors declare that they have no conflict of interest.*

Acknowledgements *This work was supported by the National Natural Science Foundation of China (82103282), Higher Education Disciplinary Innovation Program (D20036), Henan Province Medical Science and Technology Research Plan (SBGJ202103061, LHGJ20190135), "Science and Technology to create Central Plains" Young Talent Lifting Project (2023HYTP041)，Henan Charity General Federation of Hepatobiliary Care Fund (GDXZ2023002).*

References

Berardi, D.E., Bock-Hughes, A., Terry, A.R., Drake, L.E., Bozek, G., and Macleod, K.F. (2022). Lipid droplet turnover at the lysosome inhibits growth of hepatocellular carcinoma in a BNIP3-dependent manner. Sci Adv 8, eabo2510.

Cao, F., Luo, A., and Yang, C. (2021). G6PD inhibits ferroptosis in hepatocellular carcinoma by targeting cytochrome P450 oxidoreductase. Cell Signal 87, 110098.

Cao, Y., Ding, W., Zhang, J., Gao, Q., Yang, H., Cao, W., Wang, Z., Fang, L., and Du, R. (2019). Significant Down-Regulation of Urea Cycle Generates Clinically Relevant Proteomic Signature in Hepatocellular Carcinoma Patients with Macrovascular Invasion. J Proteome Res 18, 2032-2044.

Chao, T., Liu, Z., Zhang, Y., Zhang, L., Huang, R., He, L., Gu, Y., Chen, Z., Zheng, Q., Shi, L., Zheng, W., Qi, X., Kong, E., Zhang, Z., Lawrence, T., Liang, Y., and Lu, L. (2019). Precise and Rapid Validation of Candidate Gene by Allele Specific Knockout With CRISPR/Cas9 in Wild Mice. Front Genet 10, 124.

Che, N., Ng, K.Y., Wong, T.L., Tong, M., Kau, P.W., Chan, L.H., Lee, T.K., Huen, M.S., Yun, J.P., and Ma, S. (2021). PRMT6 deficiency induces autophagy in hostile microenvironments of hepatocellular carcinoma tumors by regulating BAG5-associated HSC70 stability. Cancer Lett 501, 247-262.

Dai, X., Xin, Y., Xu, W., Tian, X., Wei, X., and Zhang, H. (2021). CBP-mediated Slug acetylation stabilizes Slug and promotes EMT and migration of breast cancer cells. Sci China Life Sci 64, 563-574.

Feng, J., Dang, Y., Zhang, W., Zhao, X., Zhang, C., Hou, Z., Jin, Y., McNutt, M.A., Marks, A.R., and Yin, Y. (2019). PTEN arginine methylation by PRMT6 suppresses PI3K-AKT signaling and modulates pre-mRNA splicing. Proc Natl Acad Sci U S A 116, 6868-6877.

Gao, J., Zhang, H.P., Sun, Y.H., Guo, W.Z., Li, J., Tang, H.W., Guo, D.F., Zhang, J.K., Shi, X.Y., Yu, D.S., Zhang, X.D., Wen, P.H., Shi, J.H., and Zhang, S.J. (2020). Synaptopodin-2 promotes hepatocellular carcinoma metastasis via calcineurin-induced nuclear-cytoplasmic translocation. Cancer Lett 482, 8-18.

Garrido, F., Pacheco, M., Vargas-Martinez, R., Velasco-Garcia, R., Jorge, I., Serrano, H., Portillo, F., Vazquez, J., and Pajares, M.A. (2018). Identification of hepatic protein-protein interaction targets for betaine homocysteine S-methyltransferase. PLoS One 13, e0199472.

Grzelj, J., Mlinaric-Rascan, I., Marko, P.B., Marovt, M., Gmeiner, T., and Smid, A. (2021). Polymorphisms in GNMT and DNMT3b are associated with methotrexate treatment outcome in plaque psoriasis. Biomed Pharmacother 138, 111456.

Gupta, C., Vikram, A., Tripathi, D.N., Ramarao, P., and Jena, G.B. (2010). Antioxidant and antimutagenic effect of

quercetin against DEN induced hepatotoxicity in rat. Phytother Res 24, 119-128.
Haberl, E.M., Pohl, R., Rein-Fischboeck, L., Horing, M., Krautbauer, S., Liebisch, G., and Buechler, C. (2021). Accumulation of cholesterol, triglycerides and ceramides in hepatocellular carcinomas of diethylnitrosamine injected mice. Lipids Health Dis 20, 135.
Huang, R., Guo, G., Lu, L., Fu, R., Luo, J., Liu, Z., Gu, Y., Yang, W., Zheng, Q., Chao, T., He, L., Wang, Y., Niu, Z., Wang, H., Lawrence, T., Malissen, M., Malissen, B., Liang, Y., and Zhang, L. (2019). The three members of the Vav family proteins form complexes that concur to foam cell formation and atherosclerosis. J Lipid Res 60, 2006-2019.
Jin, R., McConnell, R., Catherine, C., Xu, S., Walker, D.I., Stratakis, N., Jones, D.P., Miller, G.W., Peng, C., Conti, D.V., Vos, M.B., and Chatzi, L. (2020). Perfluoroalkyl substances and severity of nonalcoholic fatty liver in Children: An untargeted metabolomics approach. Environ Int 134, 105220.
Kim, H., Barua, A., Huang, L., Zhou, T., Bolaji, M., Zachariah, S., Mitra, A., Jung, S.Y., He, B., and Feng, Q. (2023). The cancer testis antigen TDRD1 regulates prostate cancer proliferation by associating with the snRNP biogenesis machinery. Oncogene.
Koh, C.M., Bezzi, M., Low, D.H., Ang, W.X., Teo, S.X., Gay, F.P., Al-Haddawi, M., Tan, S.Y., Osato, M., Sabo, A., Amati, B., Wee, K.B., and Guccione, E. (2015). MYC regulates the core pre-mRNA splicing machinery as an essential step in lymphomagenesis. Nature 523, 96-100.
Lee, S.H., So, J., and Shin, D. (2023). Hepatocyte-to-cholangiocyte conversion occurs through transdifferentiation independently of proliferation in zebrafish. Hepatology 77, 1198-1210.
Li, G., Li, X., Zhuang, S., Wang, L., Zhu, Y., Chen, Y., Sun, W., Wu, Z., Zhou, Z., Chen, J., Huang, X., Wang, J., Li, D., Li, W., Wang, H., and Wei, W. (2022a). Gene editing and its applications in biomedicine. Sci China Life Sci 65, 660-700.
Li, M., He, X., Guo, W., Yu, H., Zhang, S., Wang, N., Liu, G., Sa, R., Shen, X., Jiang, Y., Tang, Y., Zhuo, Y., Yin, C., Tu, Q., Li, N., Nie, X., Li, Y., Hu, Z., Zhu, H., Ding, J., Li, Z., Liu, T., Zhang, F., Zhou, H., Li, S., Yue, J., Yan, Z., Cheng, S., Tao, Y., and Yin, H. (2020). Aldolase B suppresses hepatocellular carcinogenesis by inhibiting G6PD and pentose phosphate pathways. Nat Cancer 1, 735-747.
Li, Q., Zhang, L., Yang, Q., Li, M., Pan, X., Xu, J., Zhong, C., Yao, F., Zhang, R., Zhou, S., Dai, X., Shi, X., Dai, Y., Xu, J., Cheng, X., Xiao, W., She, Z., Wang, K., Qian, X., Pu, L., Zhang, P., and Wang, X. (2023a). Thymidine kinase 1 drives hepatocellular carcinoma in enzyme-dependent and -independent manners. Cell Metab.
Li, S.Y., Zhu, Y., Li, R.N., Huang, J.H., You, K., Yuan, Y.F., and Zhuang, S.M. (2021). LncRNA Lnc-APUE is Repressed by HNF4alpha and Promotes G1/S Phase Transition and Tumor Growth by Regulating MiR-20b/E2F1 Axis. Adv Sci (Weinh) 8, 2003094.
Li, T., Qian, C., Gu, Y., Zhang, J., Li, S., and Xia, N. (2023b). Current progress in the development of prophylactic and therapeutic vaccines. Sci China Life Sci 66, 679-710.
Li, Y., Jiang, W., Feng, Y., Wu, L., Jia, Y., and Zhao, R. (2022b). Betaine Alleviates High-Fat Diet-Induced Disruptionof Hepatic Lipid and Iron Homeostasis in Mice. Int J Mol Sci 23.
Liu, C., Zou, W., Nie, D., Li, S., Duan, C., Zhou, M., Lai, P., Yang, S., Ji, S., Li, Y., Mei, M., Bao, S., Jin, Y., and Pan, J. (2022). Loss of PRMT7 reprograms glycine metabolism to selectively eradicate leukemia stem cells in CML. Cell Metab 34, 818-835 e817.
Liu, R., Li, W., Tao, B., Wang, X., Yang, Z., Zhang, Y., Wang, C., Liu, R., Gao, H., Liang, J., and Yang, W. (2019). Tyrosine phosphorylation activates 6-phosphogluconate dehydrogenase and promotes tumor growth and radiation resistance. Nat Commun 10, 991.
Liu, X., He, J., Mao, L., Zhang, Y., Cui, W., Duan, S., Jiang, A., Gao, Y., Sang, Y., and Huang, G. (2021). EPZ015666, a selective protein arginine methyltransferase 5 (PRMT5) inhibitor with an antitumour effect in retinoblastoma. Exp Eye Res 202, 108286.
Lupu, D.S., Orozco, L.D., Wang, Y., Cullen, J.M., Pellegrini, M., and Zeisel, S.H. (2017). Altered methylation of specific DNA loci in the liver of Bhmt-null mice results in repression of Iqgap2 and F2rl2 and is associated with development of preneoplastic foci. FASEB J 31, 2090-2103.
Ma, H., Zhang, F., Zhou, L., Cao, T., Sun, D., Wen, S., Zhu, J., Xiong, Z., Tsau, M.T., Cheng, M.L., Hung, L.M., Zhou, Y., and Li, Q. (2021). c-Src facilitates tumorigenesis by phosphorylating and activating G6PD. Oncogene 40, 2567-2580.
Min, H.Y., Lee, H.J., Suh, Y.A., Pei, H., Kwon, H., Jang, H.J., Yun, H.J., Moon, H.G., and Lee, H.Y. (2022). Targeting epidermal growth factor receptor in paclitaxel-resistant human breast and lung cancer cells with

upregulated glucose-6-phosphate dehydrogenase. Br J Cancer 127, 661-674.
Ni, Y., Yang, Z., Agbana, Y.L., Bai, H., Wang, L., Yang, L., Yi, Z., Cheng, J., Zhang, Q., Kuang, Y., and Zhu, Y. (2021). Silent information regulator 2 promotes clear cell renal cell carcinoma progression through deacetylation and small ubiquitin-related modifier 1 modification of glucose 6-phosphate dehydrogenase. Cancer Sci 112, 4075-4086.
Owumi, S.E., Olugbami, J.O., Akinnifesi, A.O., and Odunola, O.A. (2021). Leaf paste of Telfairia occidentalis favourably modulates deleterious effects associated with exposure to diethylnitrosamine in male Wistar rats. J Complement Integr Med.
Qi, X., Chen, S., He, H., Wen, W., and Wang, H. (2021). The role and potential application of extracellular vesicles in liver cancer. Sci China Life Sci 64, 1281-1294.
Qiu, P., Sun, J., Man, S., Yang, H., Ma, L., Yu, P., and Gao, W. (2017). Curcumin Attenuates N-Nitrosodiethylamine-Induced Liver Injury in Mice by Utilizing the Method of Metabonomics. J Agric Food Chem 65, 2000-2007.
Roy, D.G., Chen, J., Mamane, V., Ma, E.H., Muhire, B.M., Sheldon, R.D., Shorstova, T., Koning, R., Johnson, R.M., Esaulova, E., Williams, K.S., Hayes, S., Steadman, M., Samborska, B., Swain, A., Daigneault, A., Chubukov, V., Roddy, T.P., Foulkes, W., Pospisilik, J.A., Bourgeois-Daigneault, M.C., Artyomov, M.N., Witcher, M., Krawczyk, C.M., Larochelle, C., and Jones, R.G. (2020). Methionine Metabolism Shapes T Helper Cell Responses through Regulation of Epigenetic Reprogramming. Cell Metab 31, 250-266 e259.
Saw, P.E., Xu, X., Chen, J., and Song, E.W. (2021). Non-coding RNAs: the new central dogma of cancer biology. Sci China Life Sci 64, 22-50.
Seyfried, N.T., Huysentruyt, L.C., Atwood, J.A., 3rd, Xia, Q., Seyfried, T.N., and Orlando, R. (2008). Up-regulation of NG2 proteoglycan and interferon-induced transmembrane proteins 1 and 3 in mouse astrocytoma: a membrane proteomics approach. Cancer Lett 263, 243-252.
Shen, X., Zhang, Y., Zhang, X., Yao, Y., Zheng, Y., Cui, X., Liu, C., Wang, Q., and Li, J.Z. (2019). Long non-coding RNA Bhmt-AS attenuates hepatic gluconeogenesis via modulation of Bhmt expression. Biochem Biophys Res Commun 516, 215-221.
Shi, Y., Niu, Y., Yuan, Y., Li, K., Zhong, C., Qiu, Z., Li, K., Lin, Z., Yang, Z., Zuo, D., Qiu, J., He, W., Wang, C., Liao, Y., Wang, G., Yuan, Y., and Li, B. (2023). PRMT3-mediated arginine methylation of IGF2BP1 promotes oxaliplatin resistance in liver cancer. Nat Commun 14, 1932.
Singh, P., Charles, S., Madhavan, T., Munusamy-Ramanujam, G., Saraswathi, N.T., Arasu, M.V., Al-Dhabi, N.A., Arshad, A., Arockiaraj, J., and Mala, K. (2021). Pharmacologic downregulation of protein arginine methyltransferase1 expression by adenosine dialdehyde increases cell senescence in breast cancer. Eur J Pharmacol 891, 173697.
Singhal, N.K., Sternbach, S., Fleming, S., Alkhayer, K., Shelestak, J., Popescu, D., Weaver, A., Clements, R., Wasek, B., Bottiglieri, T., Freeman, E.J., and McDonough, J. (2020). Betaine restores epigenetic control and supports neuronal mitochondria in the cuprizone mouse model of multiple sclerosis. Epigenetics 15, 871-886.
Sternbach, S., West, N., Singhal, N.K., Clements, R., Basu, S., Tripathi, A., Dutta, R., Freeman, E.J., and McDonough, J. (2021). The BHMT-betaine methylation pathway epigenetically modulates oligodendrocyte maturation. PLoS One 16, e0250486.
Tang, S., Cao, Y., Cai, Z., Nie, X., Ruan, J., Zhou, Z., Ruan, G., Zhu, Z., Han, W., and Ding, C. (2022). The lncRNA PILA promotes NF-kappaB signaling in osteoarthritis by stimulating the activity of the protein arginine methyltransferase PRMT1. Sci Signal 15, eabm6265.
Teesalu, M., Rovenko, B.M., and Hietakangas, V. (2017). Salt-Inducible Kinase 3 Provides Sugar Tolerance by Regulating NADPH/NADP(+) Redox Balance. Curr Biol 27, 458-464.
Teng, Y.W., Ellis, J.M., Coleman, R.A., and Zeisel, S.H. (2012). Mouse betaine-homocysteine S-methyltransferase deficiency reduces body fat via increasing energy expenditure and impairing lipid synthesis and enhancing glucose oxidation in white adipose tissue. J Biol Chem 287, 16187-16198.
Teng, Y.W., Mehedint, M.G., Garrow, T.A., and Zeisel, S.H. (2011). Deletion of betaine-homocysteine S-methyltransferase in mice perturbs choline and 1-carbon metabolism, resulting in fatty liver and hepatocellular carcinomas. J Biol Chem 286, 36258-36267.
Ti, D., Bai, M., Li, X., Wei, J., Chen, D., Wu, Z., Wang, Y., and Han, W. (2021). Adaptive T cell immunotherapy in cancer. Sci China Life Sci 64, 363-371.
Tsuchiya, H., da Costa, K.A., Lee, S., Renga, B., Jaeschke, H., Yang, Z., Orena, S.J., Goedken, M.J., Zhang, Y.,

Kong, B., Lebofsky, M., Rudraiah, S., Smalling, R., Guo, G., Fiorucci, S., Zeisel, S.H., and Wang, L. (2015). Interactions Between Nuclear Receptor SHP and FOXA1 Maintain Oscillatory Homocysteine Homeostasis in Mice. Gastroenterology 148, 1012-1023 e1014.
Wang, M., Hu, J., Yan, L., Yang, Y., He, M., Wu, M., Li, Q., Gong, W., Yang, Y., Wang, Y., Handy, D.E., Lu, B., Hao, C., Wang, Q., Li, Y., Hu, R., Stanton, R.C., and Zhang, Z. (2019). High glucose-induced ubiquitination of G6PD leads to the injury of podocytes. FASEB J 33, 6296-6310.
Wang, Y.P., Zhou, L.S., Zhao, Y.Z., Wang, S.W., Chen, L.L., Liu, L.X., Ling, Z.Q., Hu, F.J., Sun, Y.P., Zhang, J.Y., Yang, C., Yang, Y., Xiong, Y., Guan, K.L., and Ye, D. (2014). Regulation of G6PD acetylation by SIRT2 and KAT9 modulates NADPH homeostasis and cell survival during oxidative stress. EMBO J 33, 1304-1320.
Whitburn, J., Rao, S.R., Morris, E.V., Tabata, S., Hirayama, A., Soga, T., Edwards, J.R., Kaya, Z., Palmer, C., Hamdy, F.C., and Edwards, C.M. (2022). Metabolic profiling of prostate cancer in skeletal microenvironments identifies G6PD as a key mediator of growth and survival. Sci Adv 8, eabf9096.
Wisniewski, J.R., Zougman, A., Nagaraj, N., and Mann, M. (2009). Universal sample preparation method for proteome analysis. Nat Methods 6, 359-362.
Wojtala, M., Rybaczek, D., Wielgus, E., Sobalska-Kwapis, M., Strapagiel, D., and Balcerczyk, A. (2021). The Role of Lysine-Specific Demethylase 1 (LSD1) in Shaping the Endothelial Inflammatory Response. Cell Physiol Biochem 55, 569-589.
Xu, W., Deng, B., Lin, P., Liu, C., Li, B., Huang, Q., Zhou, H., Yang, J., and Qu, L. (2020). Ribosome profiling analysis identified a KRAS-interacting microprotein that represses oncogenic signaling in hepatocellular carcinoma cells. Sci China Life Sci 63, 529-542.
Yamawaki, K., Mori, Y., Sakai, H., Kanda, Y., Shiokawa, D., Ueda, H., Ishiguro, T., Yoshihara, K., Nagasaka, K., Onda, T., Kato, T., Kondo, T., Enomoto, T., and Okamoto, K. (2021). Integrative analyses of gene expression and chemosensitivity of patient-derived ovarian cancer spheroids link G6PD-driven redox metabolism to cisplatin chemoresistance. Cancer Lett 521, 29-38.
Yang, X., Zeng, Z., Jie, X., Wang, Y., Han, J., Zheng, Z., Li, J., Liu, H., Dong, X., Wu, G., and Xu, S. (2022). Arginine methyltransferase PRMT5 methylates and destabilizes Mxi1 to confer radioresistance in non-small cell lung cancer. Cancer Lett 532, 215594.
Yin, S., Liu, L., Ball, L.E., Wang, Y., Bedford, M.T., Duncan, S.A., Wang, H., and Gan, W. (2023). CDK5-PRMT1-WDR24 signaling cascade promotes mTORC1 signaling and tumor growth. Cell Rep 42, 112316.
Yin, S., Liu, L., Brobbey, C., Palanisamy, V., Ball, L.E., Olsen, S.K., Ostrowski, M.C., and Gan, W. (2021). PRMT5-mediated arginine methylation activates AKT kinase to govern tumorigenesis. Nat Commun 12, 3444.
Yin, S., Ma, L., Shao, T., Zhang, M., Guan, Y., Wang, L., Hu, Y., Chen, X., Han, H., Shen, N., Qiu, W., Geng, H., Yu, Y., Li, S., Yu, W., Liu, M., and Li, D. (2022). Enhanced genome editing to ameliorate a genetic metabolic liver disease through co-delivery of adeno-associated virus receptor. Sci China Life Sci 65, 718-730.
Zeng, C., Ouyang, J., Sun, L., Zeng, Z., Tan, Y., Zeng, F., and Wu, S. (2022). An activatable probe for detection and therapy of food-additive-related hepatic injury via NIR-II fluorescence/optoacoustic imaging and biomarker-triggered drug release. Anal Chim Acta 1208, 339831.
Zhang, L., He, Y., Jiang, Y., Wu, Q., Liu, Y., Xie, Q., Zou, Y., Wu, J., Zhang, C., Zhou, Z., Bian, X.W., and Jin, G. (2023). PRMT1 reverts the immune escape of necroptotic colon cancer through RIP3 methylation. Cell Death Dis 14, 233.
Zhang, Y., Xu, Y., Lu, W., Ghergurovich, J.M., Guo, L., Blair, I.A., Rabinowitz, J.D., and Yang, X. (2021). Upregulation of Antioxidant Capacity and Nucleotide Precursor Availability Suffices for Oncogenic Transformation. Cell Metab 33, 94-109 e108.
Zhou, B., Wang, Y., Zhang, L., Shi, X., Kong, H., Zhang, M., Liu, Y., Shao, X., Liu, Z., Song, H., Li, W., Gao, X., Chang, Y., Dou, C., Guo, W., Zhang, S., Kang, X., Gao, J., Liang, Y., Zheng, J., and Kong, E. (2022). The palmitoylation of AEG-1 dynamically modulates the progression of hepatocellular carcinoma. Theranostics 12, 6898-6914.
Zhou, L., Jia, X., Shang, Y., Sun, Y., Liu, Z., Liu, J., Jiang, W., Deng, S., Yao, Q., Chen, J., and Li, H. (2023). PRMT1 inhibition promotes ferroptosis sensitivity via ACSL1 upregulation in acute myeloid leukemia. Mol Carcinog.
Zhou, L., Wang, F., Sun, R., Chen, X., Zhang, M., Xu, Q., Wang, Y., Wang, S., Xiong, Y., Guan, K.L., Yang, P., Yu, H., and Ye, D. (2016). SIRT5 promotes IDH2 desuccinylation and G6PD deglutarylation to enhance cellular antioxidant defense. EMBO Rep 17, 811-822.

Zhu, Y., Liu, L., Tan, D., Sun, W., Ke, Q., Yue, X., and Bai, B. (2021). S-desulfurization: A different covalent modification mechanism from persulfidation by GSH. Free Radic Biol Med 167, 54-65.

Figure legends

Figure 1. **BHMT is poorly expressed in human HCC tissues and positively correlates with patient survival. (A–C)** Heatmap representation of differentially expressed protein **(A)**, volcano plots of all proteins **(B)**, and BHMT expression **(C)** measured by label-free protein quantification in 40 paired adjacent normal liver (N) and tumor (T) tissues of patients with HCC. **(D)** Western blot analysis of BHMT expression in 18 paired N and T tissues. **(E)** Representative IHC staining of BHMT in N and T tissues (n=6). Scale bar, 50 μm. **(F, G)** BHMT level was examined in 134 paired N and T tissues by tissue microarray immunohistochemistry **(F)** and quantitative distribution map **(G)**. Scale bar, 5000 μm. **(H)** Kaplan-Meier analysis of overall survival (left) and recurrence-free survival (right) in patients with HCC after stratification by the defined IHC score for BHMT. Statistical significance was determined using a paired two-tailed Student's t-test for comparison between two groups.

Figure 2. BHMT suppresses tumorigenicity of human HCC cells. (A, B) CCK-8 assay (n=6) and plate clone formation assay (n=3) were performed to measure cell proliferation in WT and Bhmt$^{-/-}$ hepatoma cells **(A)** and hepatoma cells bearing either pLenti-CMV-GFP-Puro or pLenti-CMV-GFP-Puro Bhmt **(B)** (n=3). **(C, D)** Representative tumor images and tumor volumes of the subcutaneous xenograft model (n=5 in each group) derived using WT and Bhmt$^{-/-}$ hepatoma cells **(C)** and WT and Bhmt hepatoma cells **(D)**. **(E–G)** Images **(E)**, volume, and weight of liver tumors using Huh7 **(F)** and HepG2 cells **(G)** for orthotopic models (n=4 in each group). Data represent the mean ± standard deviation (SD) (A, B, F, and G), or mean ± standard error (SEM) (C, D). Statistical significance was determined using two-tailed unpaired Student's t-test. *P <0.05, **P <0.01, ***P <0.001.

Figure 3. *Bhmt* suppresses tumorigenesis in DEN-induced HCC model. (A) Schematic of the generation of *Bhmt*$^{-/-}$ C57BL/6 mice. **(B)** Schematic of DEN-induced HCC model. **(C, D)** Representative images of whole liver morphology **(C)** and H&E staining of liver sections **(D)** from NaCl- and DEN-treated WT and *Bhmt*$^{-/-}$ mice. **(E)** Western blot analysis of BHMT expression in the livers of WT and *Bhmt*$^{-/-}$ mice. **(F)** Quantifications of liver/body weight ratio, tumor number, and maximum tumor volume in WT and *Bhmt*$^{-/-}$ mice treated with NaCl or DEN. **(G)** Schematic of DEN-induced HCC model mice treated with AAV8-Ctrl or AAV8-*Bhmt*. **(H, I)** Representative images of whole liver morphology **(H)** and H&E staining of liver sections **(I)** from AAV8-Ctrl or AAV8-*Bhmt* treated *Bhmt*$^{-/-}$ HCC model mice. **(J)** Flag and *BHMT* expression in the livers of the AAV8-Ctrl and AAV8-*Bhmt* groups. **(K)** Statistical analysis of liver/body weight ratio, tumor number, and maximum tumor volume in AAV8-Ctrl and AAV8-*Bhmt* treated mice. N=6 male mice per group. Data represent mean ± SD. Statistical significance was determined using two-tailed unpaired Student's t-test.

Figure 4. G6PD and PPP metabolism are activated, G6PD activity is negatively correlated with BHMT levels in patients with HCC. (A) Metabolite contents in PPP metabolism in matched tissues from patients with HCC (n=40). N, normal tissue; T, tumor. **(B)** Expression of enzymes involved in PPP metabolism in matched fresh N and T tissues (n=40). **(C)** Correlation between BHMT and key PPP enzymes (G6PD, RPE, and TKT) in N and T tissues from 40 patients with HCC. **(D, E)** Western blot analysis of G6PD expression in N and T tissues (n=18). **(F, G)** G6PD activity in N and T tissues (n=28). Statistical significance was determined using two-tailed paired Student's t-test.

Figure 5. BHMT represses PPP metabolism and G6PD activity. (A) G6PD and BHMT levels in the livers of WT and *Bhmt*$^{-/-}$ mice were detected by western blot analysis (n=6 male mice per group). **(B)** G6PD activity, 6PG content, and NADPH/NADP$^+$ ratio in the livers of WT and *Bhmt*$^{-/-}$ mice (n=6 male mice per group). **(C)** G6PD and BHMT expression in WT, Bhmt$^{-/-}$, and Bhmt hepatoma cells detected by

western blotting (*n*=3). **(D)** G6PD activity, 6PG content, NADPH/$NADP^+$ ratio (*n*=3), and intracellular ROS levels (*n*=6) in WT, $Bhmt^{-/-}$, and Bhmt hepatoma cells. **(E)** Western blot analysis of BHMT and G6PD expression in tumor-bearing nude mice via subcutaneous injection of WT, $Bhmt^{-/-}$, and Bhmt hepatoma cells (*n*=5 in each group). **(F)** G6PD activity, 6PG, and NADPH/$NADP^+$ ratio in tumor-bearing nude mice via subcutaneous injection of WT, $Bhmt^{-/-}$, and Bhmt hepatoma cells (*n*=5 in each group). Data represent mean ± SD. Statistical significance was determined by two-tailed unpaired Student's *t*-test. **P* <0.05, ***P* <0.01, ****P* <0.001, *ns*, no significance.

Figure 6. BHMT alleviates tumorigenesis by inhibiting G6PD activity and PPP metabolism. (A) G6PD activity, PPP metabolism (*n*=4) and intracellular ROS level (*n*=6) in WT, $Bhmt^{-/-}$, and Bhmt hepatoma cells treated with Sol. or 6AN (25μM). **(B)** Cell proliferation (*n*=10) and clone formation (*n*=3) in WT, $Bhmt^{-/-}$, and Bhmt hepatoma cells treated with Sol. or 25μM 6AN. **(C)** Schematic of subcutaneous tumor formation and intraperitoneal injection of Sol. or 6AN (3mg/kg) in nude mice. **(D)** WT and $Bhmt^{-/-}$ hepatoma cells were subcutaneously transplanted into the left and right flanks of BALB/c nude mice (*n*=5 per group). Tumor volume was measured every two days after intraperitoneal injection of Sol. or 6AN. **(E)** G6PD activity, 6PG and NADPH/$NADP^+$ ratio from the same experiments in **D** (*n*=5 in each group). Data represent mean ± SD (A, B, E), or mean ± SEM (D). Statistical significance was determined using two-tailed unpaired Student's *t*-test. **P* <0.05, ***P* <0.01, ****P* <0.001, *ns*, no significance.

Figure 7. Effect of BHMT on R246 methylation of G6PD. (A) The association between mono-methylation of G6PD and BHMT expression in WT, $Bhmt^{-/-}$, and Bhmt hepatoma cells analyzed by co-IP and western blotting (*n*=3). **(B)** Schematic illustrating the conserved peptide sequence, generation of site-specific antibodies against G6PD-R246 me1 and G6PD-R246 and validation of antibody specificity. **(C)** Schematic of point mutation (R246K) in exon 7 of human G6PD. **(D)** G6PD expression and R246 methylation of G6PD in HuH7 and HepG2 cells transfected with Vec, WT, or R246K plasmid (*n*=3). **(E)** Levels of mono-methylation of G6PD in hepatoma cells transfected with Vec, WT, or R246K plasmid analyzed using coIP and western blotting (*n*=3). **(F)** Mass spectrometry validation of the R246 methylation site in G6PD. Data represent mean ± SD. Statistical significance was determined using two-tailed unpaired Student's *t*-test or one-way ANOVA followed by two-tailed unpaired Student's *t*-test. **P* <0.05, ***P* <0.01, ****P* <0.001, *ns*, no significance.

Figure 8. Role of BHMT in regulating R246 methylation of G6PD. (A) G6PD expression and R246 methylation of G6PD (*n*=3), **(B)** G6PD activity (*n*=3), and **(C)** PPP metabolism (*n*=3) and intracellular ROS level (*n*=6) in WT, $Bhmt^{-/-}$, and Bhmt hepatoma cells transfected with Vec, WT, or R246K plasmid. **(D)** CCK-8 assay (*n*=6) and plate clone formation assay (*n*=3) to measure the proliferation of hepatoma cells bearing Vec, WT, or R246K plasmid. **(E)** Levels of R246 methylation of G6PD in 134 paired adjacent normal liver (N) and tumor (T) tissues using tissue microarray immunohistochemistry (left) and quantitative distribution map (right). Scale bar, 5000 μm. **(F, G)** Correlation between BHMT and R246 methylation of G6PD **(F)** and level of R246 methylation of G6PD and TNM staging **(G)** in tumor tissues from tissue microarray immunohistochemistry. **(H)** Kaplan-Meier analysis of overall survival (left) and recurrence-free survival (right) in patients with HCC after stratification by the defined IHC score for R246 methylation. **(I)** Kaplan–Meier analysis of overall survival (left) and recurrence-free survival (right) in patients with HCC after stratification by the combination of R246 methylation and BHMT expression. Data represent mean ± SD. Statistical significance was determined by one-way ANOVA followed by two-tailed unpaired Student's *t*-test. **P* <0.05, ***P* <0.01, ****P* <0.001, *ns*, no significance.

Figures

Figure 1.

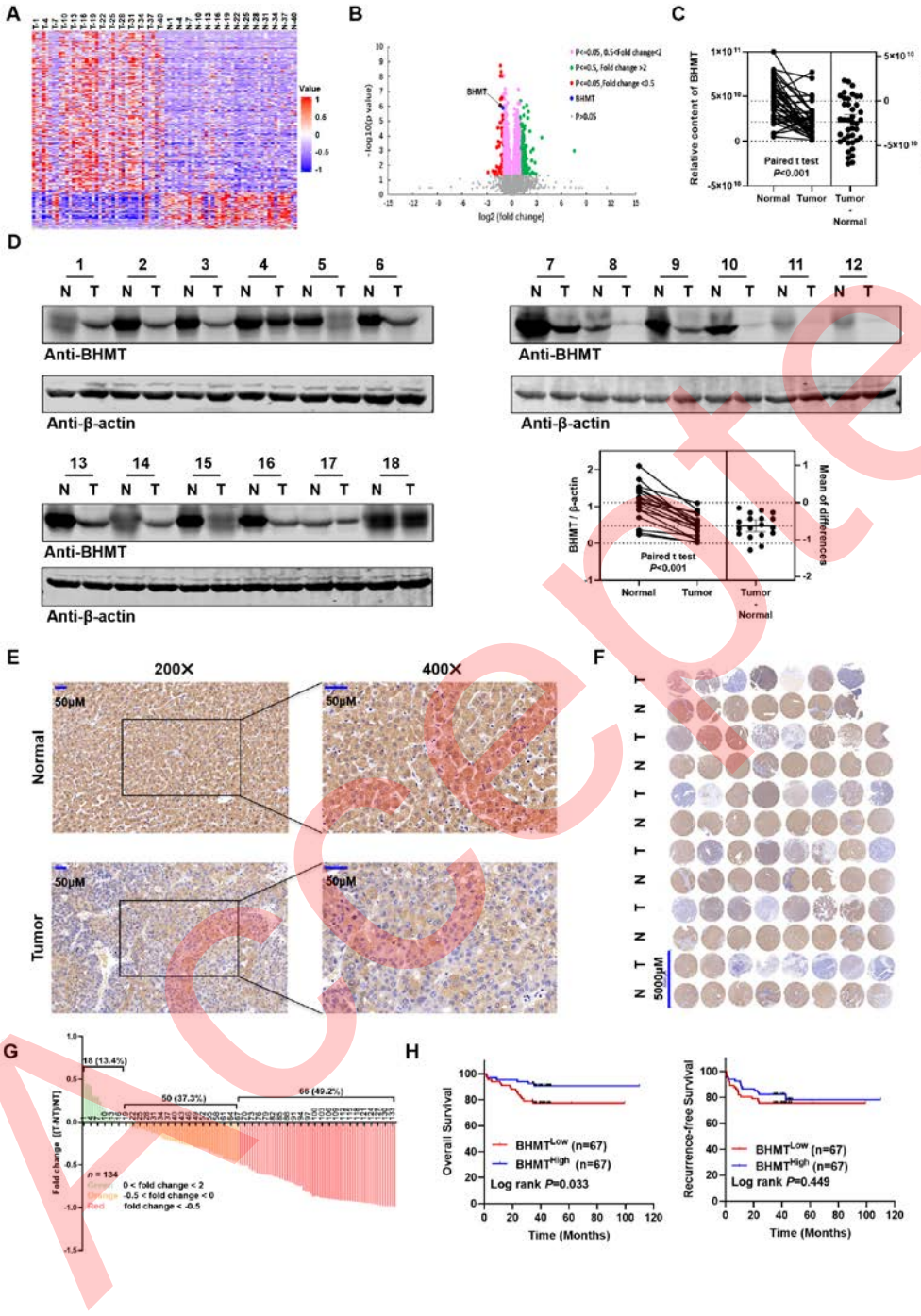

https://engine.scichina.com/doi/10.1007/s11427-023-2481-3

Figure 2.

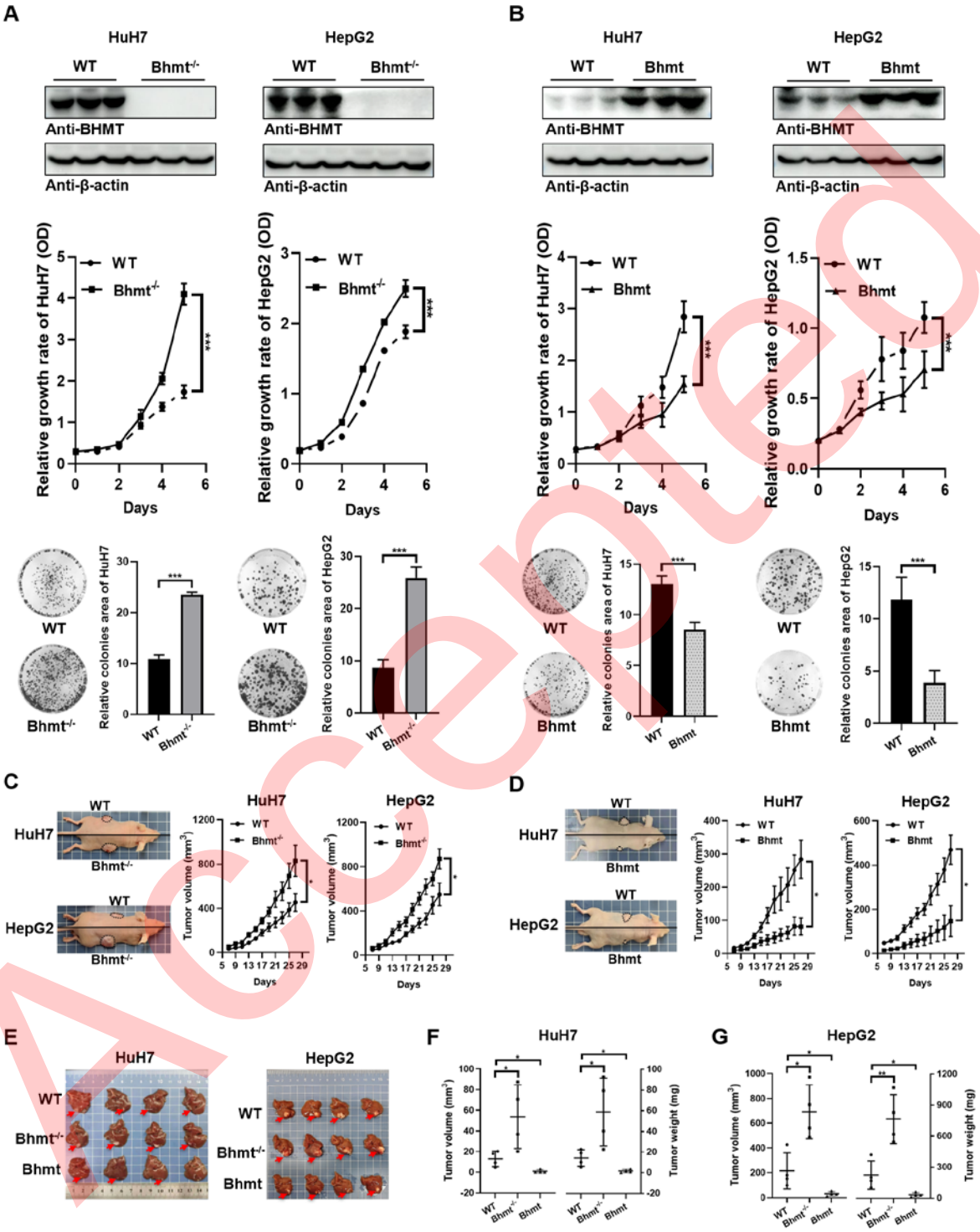

Figure 3.

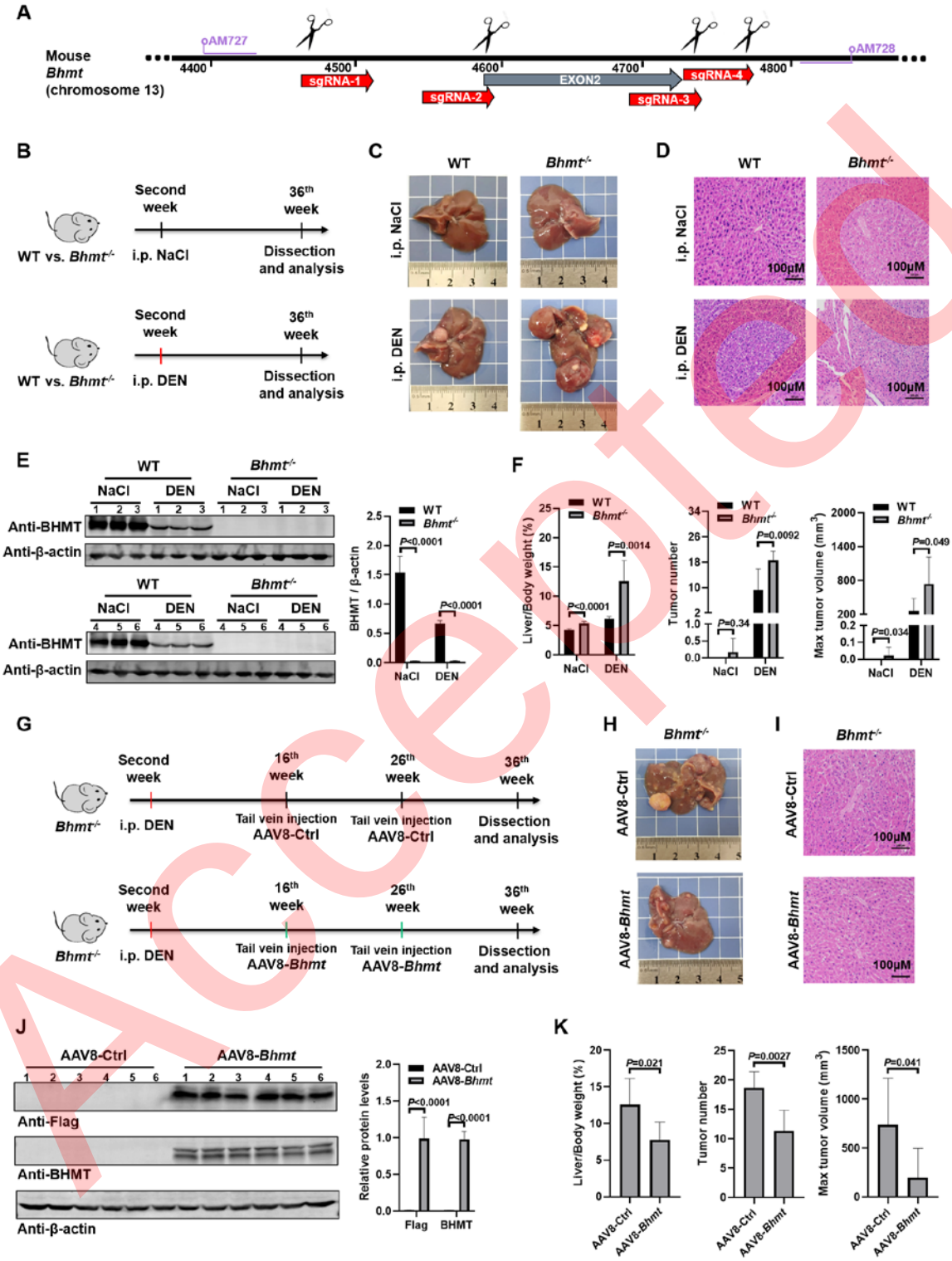

Figure 4.

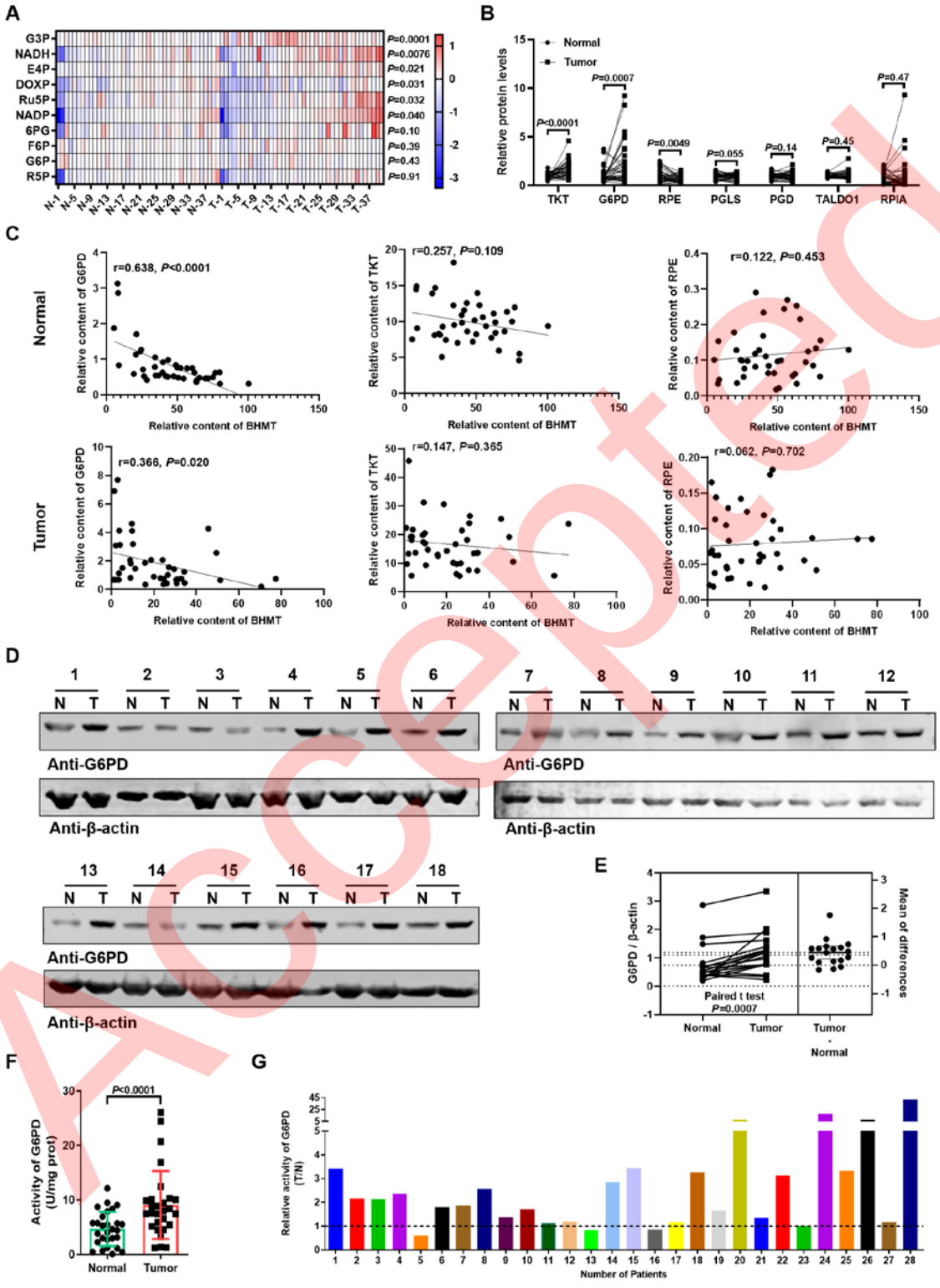

Figure 5.

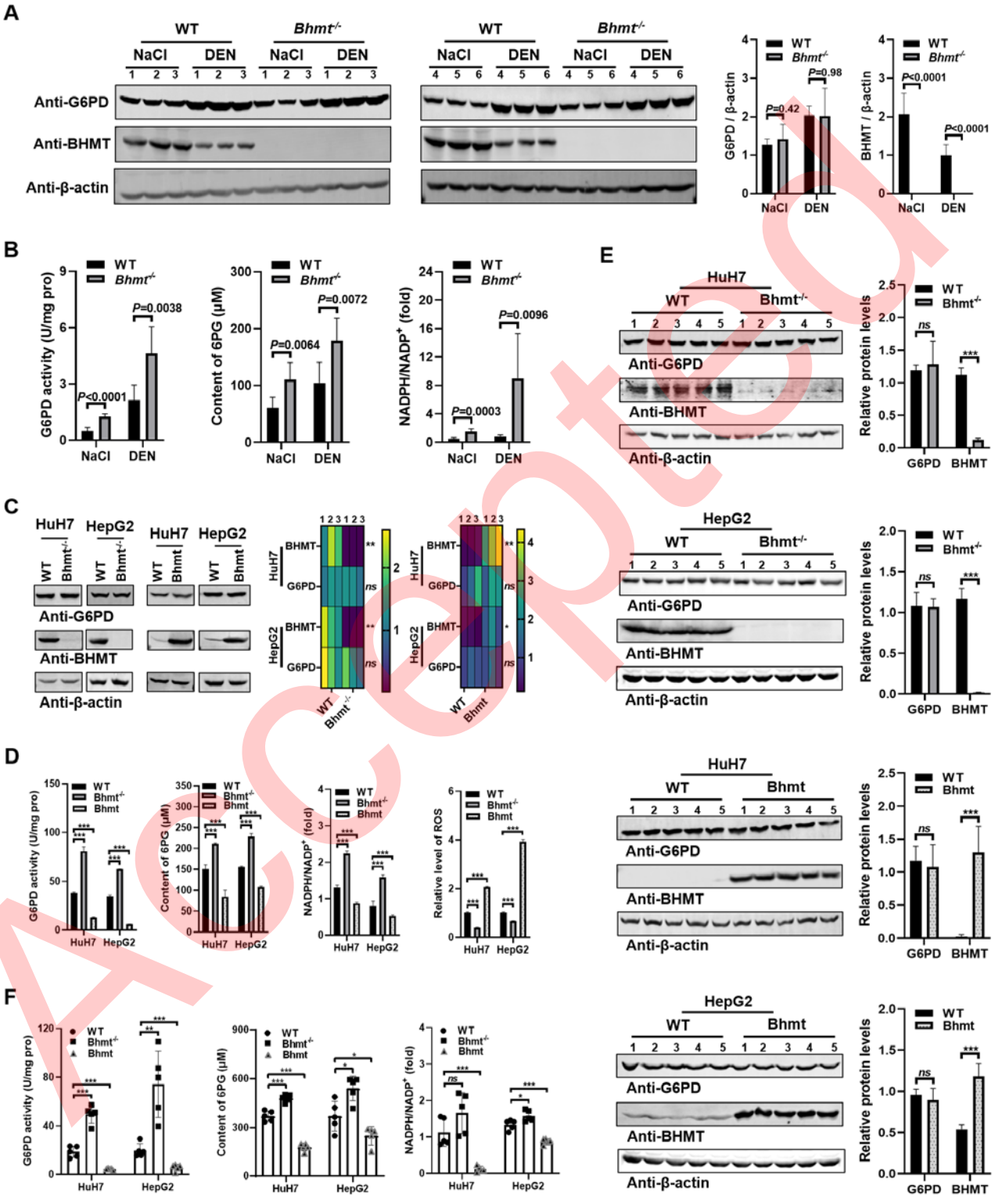

Figure 6.

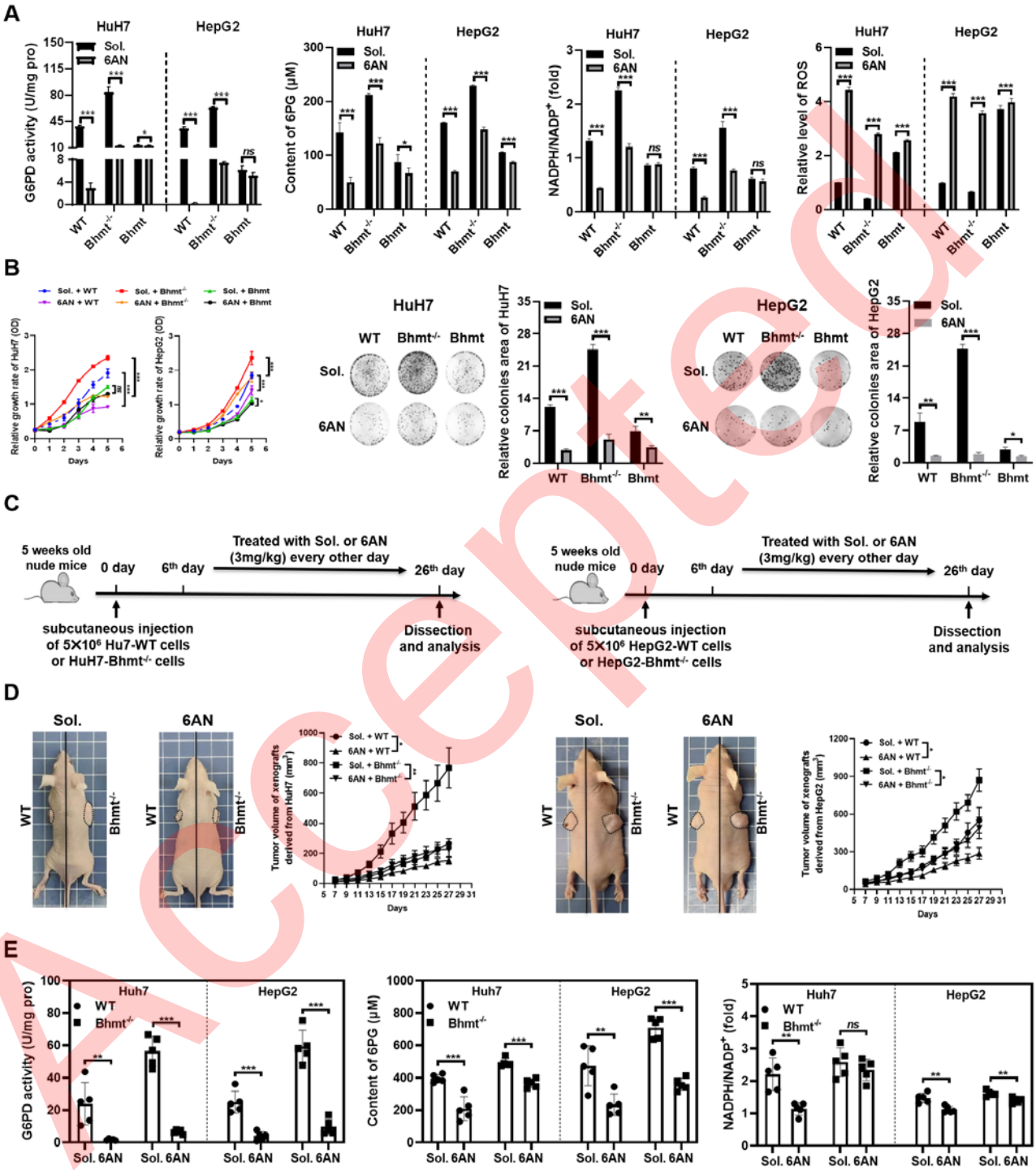

Figure 7.

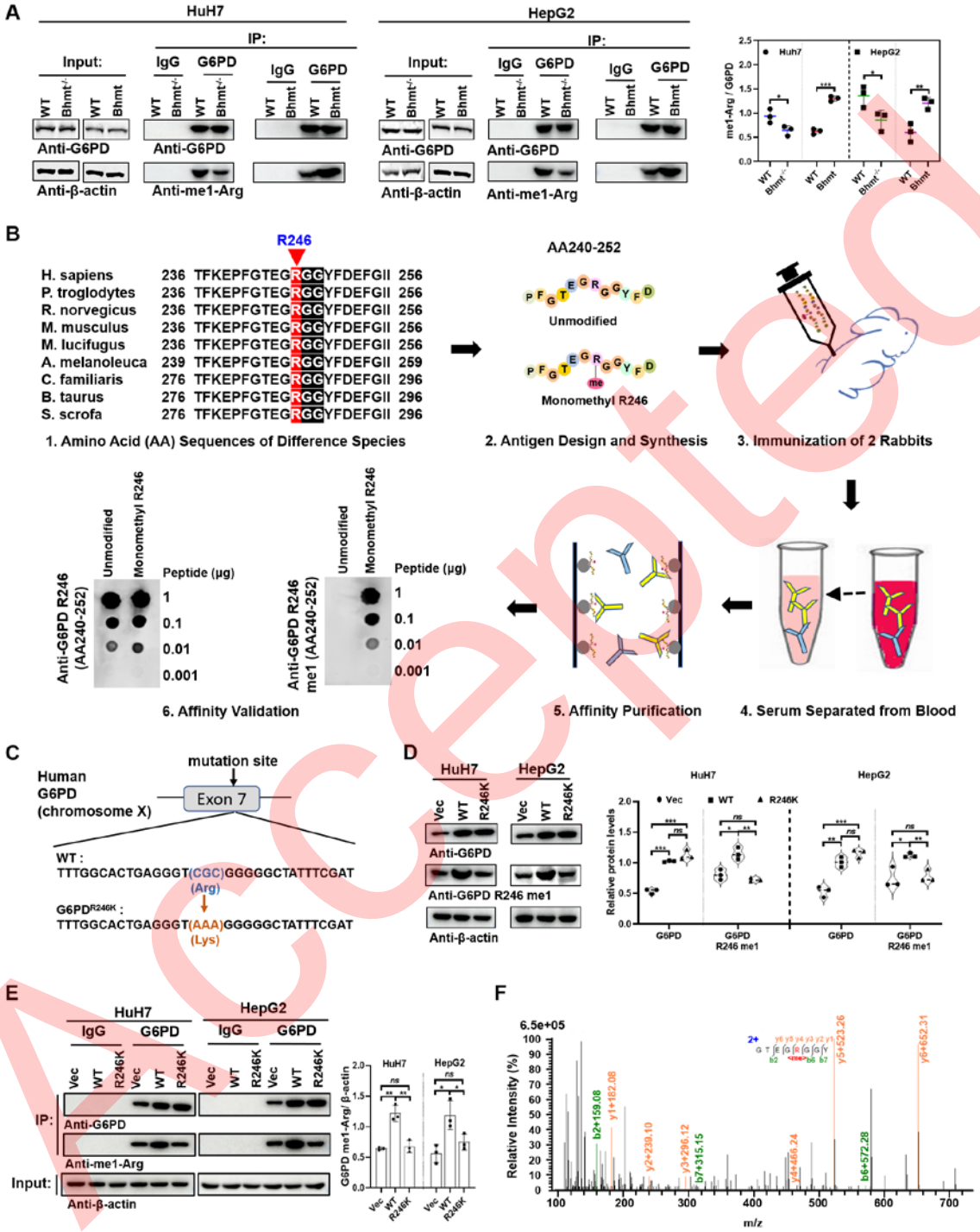

Figure 8.

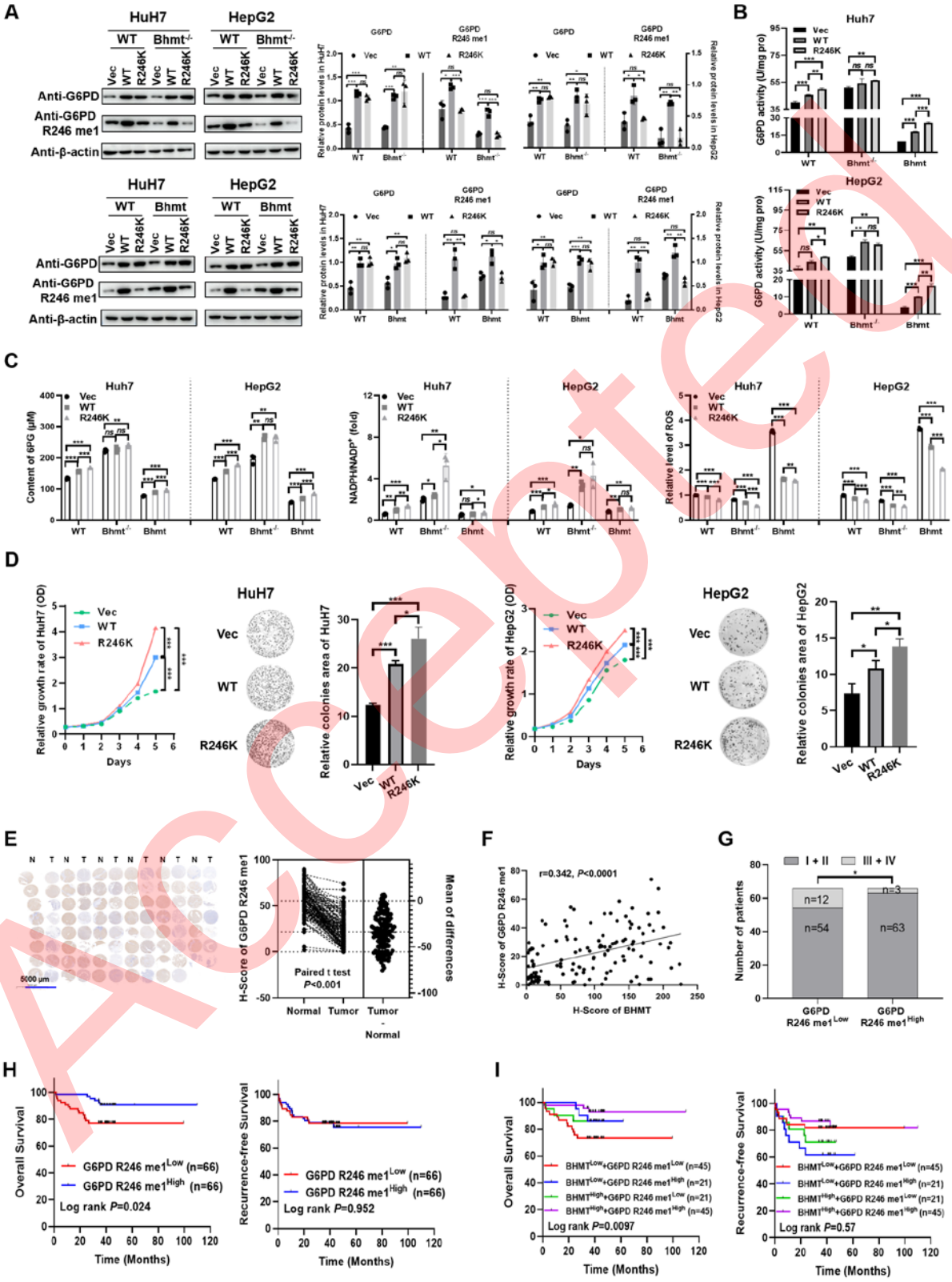

Tables

Table 1. Correlation analysis between clinical features and BHMT expression in HCC

Characteristics of patients		No. of patients	BHMT level		*P*-value
			Low	High	
Age (y)	<60	102	54	48	0.224
	≥60	32	13	19	
Sex	Male	111	53	58	0.252
	Female	23	14	9	
Alpha fetal protein level (ng/ml)	<20	52	**18**	**34**	**0.002**
	≥20	74	**46**	**28**	
Tumor size (cm)	<5	62	27	35	0.166
	≥5	72	40	32	
Number of lesions	Single	109	52	57	0.268
	Multifocal	25	15	10	
Microvascular invasion	Absent	86	**37**	**49**	**0.045**
	Present	42	**26**	**16**	
Diabetes	Absent	131	66	65	0.559
	Present	3	1	2	
Hepatitis history	Absent	54	29	25	0.481
	Present	80	38	42	
TNM tumor stage	I + II	119	59	60	0.784
	III + IV	15	8	7	